On the relevance of the lift force in bubbly turbulence

By IRENE M. MAZZITELLI[1], DETLEF LOHSE[1] AND FEDERICO TOSCHI[2]

[1]Department of Applied Physics and J. M. Burgers Centre for Fluid Dynamics,
University of Twente, 7500 AE Enschede, The Netherlands

[2]Istituto per le Applicazioni del Calcolo, CNR, Viale del Policlinico 137, 00161, Roma, Italy
and INFM, Unità di Tor Vergata, Via della Ricerca Scientifica 1, 00133, Roma, Italy

Microbubble-laden homogeneous and isotropic turbulent flow is investigated by using direct numerical simulation of the three-dimensional Navier–Stokes equations and computing the bubble trajectories with Lagrangian tracking. The bubble motion is calculated by taking into account the effect of fluid acceleration plus added mass, drag, gravity, and in particular the lift force, which had been neglected in many previous simulations. By comparing the results from simulations with and without lift, we find the effect of the lift force to be crucial: for passive bubbles, i.e. bubbles without backreaction on the flow (one-way coupling), the lift enhances the accumulation of bubbles on the downward flow side of vortices, resulting in a considerably reduced rise velocity of bubbles in turbulent flow, compared to still water. This also has consequences for the active bubble case, i.e. for bubbles with backreaction on the flow (two-way coupling): the energy spectrum of the turbulence is modified non-uniformly. Because of the combined effect of preferential bubble clustering in downflow zones and the local buoyant transfer, which reduces the vertical fluid velocity fluctuations, large-scale motions (small wavenumbers k) are suppressed. In contrast, small-scale motions (large wavenumbers k) are enhanced due to the local bubble forcing. The net effect turns out to be a reduction of the energy dissipation rate.

1. Introduction

With their ubiquitous occurrence in a multitude of fluid systems bubbles occupy a very important place in contemporary science and technology. One can readily cite many examples: the chemical industry (where gas–liquid reactors rely on bubbles to increase the contact area between the phases), the oceans (where breaking-wave-generated bubbles are important sinks for atmospheric CO_2), the production and transport of oil (where bubbles are purposely injected to help to lift thick heavy oil to the surface, or arise due to the exsolution of dissolved gases), energy generation (where boiling is the key process in producing the steam to drive turbines), and many others.

In many of these situations we have to deal with turbulent bubbly flow. The two basic questions for this type of flow are: (i) How do bubbles move within the turbulent flow? and (ii) How do they affect the turbulence?

Though it is very difficult to address these questions experimentally, much progress has been achieved since the early measurements of Snyder & Lumley (1971) and

Serizawa, Kataoka & Michiyoshi (1975*a,b,c*), see e.g. Michiyoshi & Serizawa (1986), Mudde, Groen & van den Akker (1997), Kumar, Moslemian & Dudukovic (1997), Mudde & Saito (2001) and Poorte & Biesheuvel (2002).

Different regimes are assessed in the experiments with low or high values of the particle/bubble Reynolds number, defined as $Re = 2a|\boldsymbol{v} - \boldsymbol{u}|/\nu$, with a the particle radius, $\boldsymbol{u} - \boldsymbol{v}$ the relative particle-to-fluid velocity and ν the fluid viscosity. Low Re indicates laminar flow whereas at high Re the flow surrounding the particles is turbulent and turbulent wakes eventually develop at their rear side.

In this paper we will focus mainly on three types of observables:

(i) The *bubble distribution* in the fluid: Bubbles are found to accumulate in low-pressure regions of the flow, i.e. in vortex filaments, and have even been used to characterize them and to measure their statistics, see e.g. Cadot, Douady & Couder (1995) and La Porta *et al.* (2000). Sridhar & Katz (1999) studied the interaction of bubbles at intermediate Re with vortex rings, and Rightley & Lasheras (2000) the dispersion and coupling of microbubbles with a free-shear flow. Both experiments indicate that, even at low void fractions, the effect of bubbles on the flow is significant, owing to the high level of clustering reached in low-pressure flow zones.

(ii) *Spectral information*: One of the effects of bubbles is to modify the energy spectrum of the turbulent flow. However, how the spectra are changed is very controversial. Lance & Bataille (1991) found that, at high bubble Reynolds number, for increasing gas fraction α, the Kolmogorov energy spectrum exponent $-5/3$ is progressively substituted by $-8/3$. It is argued that the steeper spectrum originates from the energy production within the bubble wakes. Figure 15 in their paper also suggests that for bubbly flow there is more spectral energy in the small-scale eddies and less in the large-scale eddies. The Taylor–Reynolds number in this experiment is $Re_\lambda = 35$. In contrast to Lance & Bataille (1991), Mudde *et al.* (1997) found the classical $-5/3$ power law in a bubble column even for a gas volume fraction of 25%, yet at high bubble Reynolds numbers. On the analytical side, L'vov, Ooms & Pomyalov (2003) have recently proposed a derivation that accounts for the spectral modulation in particle flows.

(iii) The *average bubble rise velocity*: Whereas particles are known from numerical simulations to (on average) sink faster in turbulent flow than in still water (Wang & Maxey 1993*b*; Yang & Lei 1998), Poorte & Biesheuvel (2002) recently measured experimentally that the mean rise velocity of large bubbles is significantly reduced (up to 35%) in turbulence compared to still water. On the other hand, either larger or smaller rise speeds have been experimentally found by Friedman & Katz (2002), for droplets slightly lighter than the fluid, depending on three parameters: turbulence intensity, droplet dimension and response time.

How to explain these observations? An efficient way is to follow a numerical approach.

For particle-laden turbulence, a large number of investigations is available in the literature, see e.g. Squires & Eaton (1990), Elghobashi & Truesdell (1993), Hunt, Perkins & Fung (1997), Boivin, Simonin & Squires (1998), Druzhinin & Elghobashi (1999), Druzhinin (2001), Marchioli & Soldati (2002) and Ooms *et al.* (2002), most of them assuming a point-particle approximation. The relevant forces on small, heavy particles are the Stokes drag and gravity. It is generally observed that initially uniformly distributed particles rapidly collect in low-vorticity regions (Squires & Eaton 1990). The clustering is more intense when tuning the particle parameters to the flow Kolmogorov scales. The backreaction of the particles on the fluid qualitatively depends on the ratio τ_p/τ_k, where τ_p is the particle response time and τ_k the Kolmogorov time

scale. When $\tau_p/\tau_k \sim O(1)$, particles dissipate turbulent kinetic energy (Boivin *et al.* 1998; Sundaram & Collins 1999), whereas microparticles with $\tau_p/\tau_k \ll 1$ are able to enhance the turbulence levels (Druzhinin & Elghobashi 1999; Druzhinin 2001; Ferrante & Elghobashi 2003).

For bubble-laden turbulence, the situation is even more complicated than for particle flow because of the free interface. Ideally, the Navier–Stokes equation should be solved, with the bubble–water interface treated as a free surface. However, within such an approach only about 100 bubbles can be included, see e.g. Bunner & Tryggvason (1999). Therefore, in order to numerically model turbulent multiphase flow with many bubbles, it is – just as for particle flow – common to employ a point-like approximation. It obviously works best for microbubbles, i.e. for bubbles smaller than all length scales of the turbulent flow, or, correspondingly, with a bubble Reynolds number of less than one.

The key question which arises is: What forces act on such a microbubble? This issue has been addressed both analytically (Maxey & Riley 1983; Thomas *et al.* 1984; Auton 1987; Auton, Hunt & Prud'Homme 1988) and numerically (Mei, Lawrence & Adrian 1991; Chang & Maxey 1994, 1995; Magnaudet, Rivero & Fabre 1995; Legendre & Magnaudet 1998). An excellent recent review on this subject can be found in Magnaudet & Eames (2000).

While some forces on bubbles are trivial, such as the buoyant force, other are highly controversial. This in particular holds for the lift force: commonly, it is modelled as (see e.g. Magnaudet & Eames 2000)

$$\boldsymbol{F}_L = C_L \rho_f \mathscr{V}_b \left(\boldsymbol{u} - \dot{\boldsymbol{x}}_b \right) \times \left(\nabla \times \boldsymbol{u} \right), \tag{1.1}$$

where ρ_f is the fluid density, $\mathscr{V}_b$ the volume of the bubble at position $\boldsymbol{x}_b$, and $\boldsymbol{u}(\boldsymbol{x}, t)$ the fluid velocity. It is moreover assumed that the lift force coefficient is $C_L = 1/2$ for bubble Reynolds numbers larger than one, as numerically found by Legendre & Magnaudet (1998) and Magnaudet & Eames (2000). Note that experiments by Sridhar & Katz (1995), performed at $20 < Re < 80$, suggest larger values for C_L and a fourth-root dependence on the local vorticity. This finding may be due to bubble contamination, strong shear, or other effects, but slightly different lift forces will only slightly change our results qualitatively. Moreover, Rensen *et al.* (2001) and Lohse & Prosperetti (2003) presented experimental results which show that $C_L = 1/2$ is not unreasonable.

In any case, if the lift force is relevant for bubbly flow, the microscopic lift force model for the bubble reflects in the macroscopic observables, such as the above-mentioned bubble distribution, the energy spectra, or the average bubble rise velocity.

However, most numerical simulations in the literature have completely neglected the effect of the lift force in bubbly turbulence. For example, for the analysis of decaying bubble-laden turbulence (Druzhinin & Elghobashi 1998) and for that of the effect of microbubbles on a spatially developing mixing layer (Druzhinin & Elghobashi 2001) only fluid acceleration, added mass, drag, and gravity force are considered, not lift. The strong point of those simulations however is that two-way coupling had been included, i.e. the backreaction of the bubbles on the flow. Indeed, in Druzhinin & Elghobashi (1998) the turbulence decay is found to be affected by the bubbles, namely either enhanced or reduced, depending on the initial bubble distribution. In Druzhinin & Elghobashi (2001), again under specific conditions on the inflow bubble profile, a reduction of the turbulence fluctuations across the mixing layer is measured. Other examples of two-way coupling simulations are Climent (1996) and Climent & Magnaudet (1997). In its method, the simulation of Climent & Magnaudet (1999) is

closest to ours, though a very different question is analysed, namely how a swarm of rising bubbles induces a flow in still water. It is two-dimensional and includes the lift force.

Older numerical simulations mainly employ one-way coupling, i.e. they neglect the backreaction of the bubbles on the flow and focus on clustering effects. These simulations revealed that the effect of the flow on the bubbles and the bubble accumulation in high-vorticity regions are strongest when (i) the typical bubble rise velocity v_T is comparable to the Kolmogorov velocity scale v_k and (ii) the typical bubble response time τ_b is comparable to the Kolmogorov time scale τ_k (see e.g. Wang & Maxey 1993*a*; Maxey, Chang & Wang 1994).

The kinematic simulation of Spelt & Biesheuvel (1997) also falls into the class of one-way coupling simulations. Here the fluid flow is not given by the Navier–Stokes equation, but by a sum of Fourier modes with random phases and amplitudes determined according to some given spectrum. However, what distinguishes this simulation is that it is one of the few which explicitly includes lift. The interesting finding is that the bubble rise velocity is considerably decreased in turbulence due to the lift force. In the limit of large bubble rise velocity this result can also be derived analytically.

In Mazzitelli, Lohse & Toschi (2003) we have further studied the effect of the lift force in bubbly turbulence, at low bubble Reynolds numbers, but now within a full Navier–Stokes simulation of homogeneous isotropic turbulence, either with one-way coupling or including two-way coupling. We employed the Eulerian–Lagrangian approach. The forces acting on bubbles are fluid acceleration plus added mass effects, drag, gravity, and in particular lift.

Indeed, in that paper we found that the lift force plays a prominent role in the bubble accumulation on the downflow side of vortices, leading to a reduced average bubble rise velocity. (Note that, however, the balance of drag force, gravity, and fluid acceleration preferentially occurs in downflow regions, so the bubble distribution with respect to the gravity direction was found slightly asymmetric also in simulations without lift forces.) Once the reaction of the bubbles on the carrier flow is included, an attenuation of the turbulence on large scales and an extra forcing on small scales is found.

In this present paper we will give a complete and quantitative description of our numerical simulation, focusing on the two-way coupling case. We will demonstrate that the lift force has a very crucial effect on all of the three above-mentioned observables, namely the bubble distribution in the flow, the energy spectrum, and the average bubble rise velocity. The relevance of the lift force is highlightened by comparing the results for those observables with analogous simulations without lift: for those simulations the average bubble rise velocity in turbulence is not reduced, which is in clear conflict with the experimental observations by Poorte & Biesheuvel (2002). Moreover, without lift no kinetic energy reduction on large scales is found, which is in contrast to the experimental results by Lance & Bataille (1991). Both findings highlight the crucial role of lift in bubbly turbulence.

Although the Lance & Bataille experiments were mainly performed with large bubbles, we believe that the spectral modifications will have qualitatively similar characteristics and in particular the same physical origin as for microbubbles. Larger bubbles rise much faster through the flow structures, with much less interaction. In the Lance & Bataille experiment the ratio $\beta = u_0/v_T$ between the r.m.s. fluid velocity fluctuations and the bubble rise velocity is always smaller than 0.1, so that no trapping of the bubbles in vortices can be expected, in contrast to microbubbles which are

trapped. Furthermore, owing to the large bubble Reynolds number, turbulent wakes develop at the rear of the bubbles to which a part of the energy induced by the bubbles is associated.

The paper is organized as follows. In §2 the bubble–fluid equations are presented and the numerical method is described and justified. Section 3 deals with the bubble distribution in the one-way coupling case. In §4 we study the consequences of two-way coupling on the energy spectra and the bubble rise velocity. Next, we compare the results of simulations with and without lift (§5). In §6 we analytically calculate the modification of the energy spectrum for randomly distributed bubbles. The result is a reduction for all wavevectors. This is also found in numerical simulations in which we fix the bubbles at the random initial positions, but still let them force the flow. This exercise therefore demonstrates that it is the interplay between bubble clustering and the lift force which leads to the spectral modifications observed in the full simulations. Section 7 contains conclusions.

2. Method of the numerical simulation

From a technical point of view, the two-phase system equations can be numerically implemented in two different ways. In the first way, which we will follow in this paper, each particle trajectory is individually tracked whilst the fluid Navier–Stokes equations are time advanced (Lagrangian–Eulerian approach, e.g. see Squires & Eaton (1990), Elghobashi & Truesdell (1993) and Boivin *et al.* (1998)). In the second method both the fluid and the disperse phase are treated as a 'continuum', thus space-averaged equations are specified for the particles/bubbles also (Eulerian–Eulerian or two-fluid approach, e.g. see Druzhinin & Elghobashi (1998, 2001)).

2.1. *Simulation of the fluid phase*

The fluid phase is governed by the incompressible Navier–Stokes equations:

$$\frac{\partial \boldsymbol{u}(\boldsymbol{x},t)}{\partial t} + \boldsymbol{u}(\boldsymbol{x},t) \cdot \nabla \boldsymbol{u}(\boldsymbol{x},t) = -\nabla p + \nu \Delta \boldsymbol{u}(\boldsymbol{x},t) + \boldsymbol{f}_L(\boldsymbol{x},t) + \boldsymbol{f}_b(\boldsymbol{x},t), \qquad (2.1)$$

where $\boldsymbol{u}(\boldsymbol{x},t)$ is the fluid velocity, p the kinematic pressure, ν the kinematic viscosity, $\boldsymbol{f}_L(\boldsymbol{x},t)$ the large-scale forcing, and $\boldsymbol{f}_b(\boldsymbol{x},t)$ the forcing due to the transfer of momentum between the fluid and the bubble phase. This bubble forcing will be derived in §2.2. Equation (2.1) is converted into an equation for the vector potential $\boldsymbol{b}(\boldsymbol{x},t)$, defined according to $\boldsymbol{u}(\boldsymbol{x},t) = \nabla \times \boldsymbol{b}(\boldsymbol{x},t)$,

$$\frac{\partial \boldsymbol{b}(\boldsymbol{x},t)}{\partial t} - \Delta^{-1}[\nabla \times (\boldsymbol{u}(\boldsymbol{x},t) \cdot \nabla \boldsymbol{u}(\boldsymbol{x},t))] = \nu \Delta \boldsymbol{b}(\boldsymbol{x},t) - \Delta^{-1}[\nabla \times (\boldsymbol{f}_L(\boldsymbol{x},t) + \boldsymbol{f}_b(\boldsymbol{x},t))]$$
$$(2.2)$$

and solved by full three-dimensional direct numerical simulation. The vector $\boldsymbol{b}(\boldsymbol{x},t)$ is expanded in discrete Fourier series in each direction on an equispaced grid and its equations are solved by means of the pseudo-spectral method. They are advanced in time by the second-order Adams–Bashforth scheme. The solution domain is a cube of side $L_0 = 2\pi$, subjected to periodic boundary conditions. It consists of $N^3 = 128^3$ grid points. The nonlinear term of (2.1) is evaluated in real space and, in order to control aliasing errors, the largest wavenumber represented is $k_{max} = 2N/3$, i.e. all k such that $k = |\boldsymbol{k}| > k_{max}$ are set to zero. The turbulence scales, as well as their ratios with respect to the characteristic bubble scales, are fixed in time by forcing the flow on small wavenumbers and thus sustaining a statistically stationary state. The forcing

ϵ	ν	η	τ_k	v_k	L_{xx}	τ_0	u_0	λ	Re_λ
1.0	0.007	0.024	0.084	0.29	0.5	2.2	1.2	0.37	62

TABLE 1. Fluid parameters. The energy input rate, ϵ, the viscosity, ν, and the dimension of the computational domain, $L_0 = 2\pi$, are fixed. All the other parameters follow.

applied on the $\boldsymbol{k}$ mode of the velocity field is (Grossmann & Lohse 1992):

$$\boldsymbol{f}_L(\boldsymbol{k}, t) = \epsilon \frac{\boldsymbol{u}(\boldsymbol{k}, t)}{\displaystyle\sum_{\boldsymbol{k} \in K_{in}} |\boldsymbol{u}(\boldsymbol{k}, t)|^2}, \quad \boldsymbol{k} \in K_{in}, \tag{2.3}$$

and $\boldsymbol{f}_L(\boldsymbol{k}, t) = 0$ otherwise. Here $K_{in} = \{\boldsymbol{k} \mid (L_0/2\pi)\boldsymbol{k} = \pm(-1, 2, 2), \pm(2, -1, -1) +$ Permutations$\}$ and ϵ is the energy input rate (which equals the energy dissipation rate for statistically stationary turbulence). The Kolmogorov length, time and velocity scales can be evaluated from the energy dissipation rate ϵ and the fluid kinematic viscosity ν according to $\eta = (\nu^3/\epsilon)^{1/4}$, $\tau_k = (\nu/\epsilon)^{1/2}$ and $v_k = (\epsilon\nu)^{1/4}$, respectively. Other relevant quantities are the large-scale r.m.s. velocity u_0, the large-eddy turnover time τ_0, the Taylor scale λ, and the Taylor–Reynolds number Re_λ,

$$u_0^2 = \frac{1}{3}\langle u_i u_i \rangle, \quad \tau_0 = \frac{\frac{3}{2}u_0^2}{\epsilon}, \quad \lambda = \frac{\langle u_x^2 \rangle^{1/2}}{\langle (\partial_x u_x)^2 \rangle^{1/2}}, \quad Re_\lambda = \frac{u_0 \lambda}{\nu},$$

where u_i, with $i = x, y, z$, is the ith component of the fluid velocity, and repeated indices are considered summed. The brackets $\langle \cdot \rangle$ indicate averages on time and space. A summary of the fluid parameters can be found in table 1.

It is necessary to fulfil some conditions for the simulation to correctly resolve both the large- and the small-scale motions. First, the solution domain has to be large enough to represent the energy-containing eddies. This is assured by the large ratio between the cube width, L_0, and the integral length scale,

$$L_{xx} = \frac{1}{\langle u_x^2 \rangle} \sum_{r_x=0}^{N/2} \langle u_x(0) u_x(r_x) \rangle \Delta r_x.$$

In our simulation $L_0/L_{xx} \simeq 12$. Second, the dissipative scales have to be sufficiently resolved. We have $k_{max}\eta \simeq 1.024$. Finally, the accuracy of the solution in time is guaranteed by the small Courant number $1/30$.

The code is fully parallelized, both for the fluid and the bubble evolution, and simulations are run on SGI Origin2000 on 16 processors. Communications between different processors are held by MPI (Message Passing Interface) subroutines. We use MPI parallelized FFTW and the sustained performance on the machine is about 40 Mflops per processor.

2.2. Bubble equation of motion

The motion of a particle or bubble in a turbulent flow is determined by both body and surface forces, whose form depends on the regime analysed. In the present work we focus on spherical undeformable particles of density ρ_p and radius a smaller than all the fluid length scales, at low values of the particle Reynolds number

$$Re = \frac{2a|\boldsymbol{v} - \boldsymbol{u}|}{\nu},$$

where v is the particle/bubble velocity and $v - u$ its relative velocity with respect to the flow. The equation of motion is given by Newton's second law, which for particles or bubbles is (see e.g. Thomas *et al.* 1984; Climent 1996; Spelt & Biesheuvel 1997)

$$\rho_p \mathscr{V}_p \frac{\mathrm{d}v}{\mathrm{d}t} = (\rho_p - \rho_f)\mathscr{V}_p g - C_D \frac{\pi a^2}{2}\rho_f |v - u|(v - u)$$

$$+ \rho_f \mathscr{V}_p \left(C_M \frac{\mathrm{D}u}{\mathrm{D}t} - \frac{\mathrm{d}v}{\mathrm{d}t} \right) + \rho_f \mathscr{V}_p \frac{\mathrm{D}u}{\mathrm{D}t} - C_L \rho_f \mathscr{V}_p (v - u) \times \boldsymbol{\omega}. \quad (2.4)$$

Here $\mathscr{V}_p = 4\pi a^3/3$ is the particle volume, ρ_f the fluid density, u the fluid velocity, and $\boldsymbol{\omega} = \nabla \times u$ the vorticity. The forces on the right-hand side of (2.4) are gravity, drag, added mass, fluid acceleration and lift, and C_D, C_M and C_L are the corresponding coefficients. We assume, in our reference frame, that gravity is directed along the negative z-axis. When Re is smaller than 1 the drag coefficient is fixed by the relation (Hadamard 1911; Ribczynski 1911)

$$C_D = \frac{16}{Re}\left(\frac{1 + (3\mu_p)/(2\mu_f)}{1 + \mu_p/\mu_f} \right). \quad (2.5)$$

The added mass coefficient for a sphere is $C_M = 1/2$ (Taylor 1928; Batchelor 1967), independent of the Reynolds number and of non-uniformities of the flow (Auton *et al.* 1988; Rivero, Magnaudet & Fabre 1991; Chang & Maxey 1995; Magnaudet *et al.* 1995).

Note that for heavy particles ($\rho_p/\rho_f \gg 1$) at low Reynolds number ($Re \ll 1$), the relevant forces in (2.4) reduce to drag and gravity, whereas for bubbles of nearly negligible density ($\rho_p/\rho_f \simeq 0$) the fluid inertia forces are also significant.

The analysis of a surfactant-free bubble, with zero-shear-stress boundary condition at the interface, is carried out by inserting $\rho_p = 0$ into (2.4). In this case, from (2.5), one finds $C_D = 16/Re$ for very small Re, whereas at intermediate Reynolds numbers ($1 < Re < 60$) corrective expressions have been found through direct numerical simulation (Mei, Klausner & Lawrence 1994; Magnaudet *et al.* 1995).

The behaviour at low to moderate Reynolds number of the lift coefficient C_L is shown in figure 17 of Legendre & Magnaudet (1998). Except of the regime $Re \ll 1$, where it displays a steep decrease as a function of Re, the high-Reynolds-number value $C_L = 1/2$ (Auton 1987) seems to be a reasonable approximation, even when $Re \sim O(1)$ (see the discussion below (1.1)).

We restrict ourselves to Reynolds number order of one and neglect all finite Reynolds number corrections, i.e. we take $C_D = 16/Re$ and $C_L = C_M = 1/2$. The resulting bubble motion equation is then

$$\frac{\mathrm{d}v}{\mathrm{d}t} = 3\frac{\mathrm{D}u}{\mathrm{D}t} - \frac{1}{\tau_b}(v - u) - 2g - (v - u) \times \boldsymbol{\omega}. \quad (2.6)$$

Here

$$\tau_b = \frac{a^2}{6\nu}$$

is the bubble time scale; the corresponding rise speed in still fluid is

$$v_T = 2g\tau_b = \frac{ga^2}{3\nu}.$$

Bubble–bubble direct interactions are neglected as we consider only low void fractions.

The trajectory $\boldsymbol{x}(t)$ of each bubble is computed using Lagrangian tracking. The bubble's velocity is advanced in time by an explicit forward Euler scheme,

$$v_i(t + \mathrm{d}t) = v_i(t) + \frac{\mathrm{d}v_i(t)}{\mathrm{d}t}\,\mathrm{d}t,$$

$$x_i(t + \mathrm{d}t) = x_i(t) + v_i(t)\,\mathrm{d}t + \frac{1}{2}\frac{\mathrm{d}v_i(t)}{\mathrm{d}t}\,\mathrm{d}t^2, \quad i = x, y, z.$$

The same time step $\mathrm{d}t$ as for the integration of the Navier–Stokes equations is applied. It fulfils the constraint $\mathrm{d}t \ll \tau_b$. In general, the bubble's instantaneous location does not coincide with a grid point. Therefore the fluid velocity and the forces, which are required to integrate (2.6), are estimated between the grid points by third-order Taylor series interpolation with 13 points (Yeung & Pope 1988). This scheme is preferred to simple linear interpolation because it gives a better description of the velocity fluctuations at high wavenumbers, to which bubble motion is rather sensitive, see Maxey *et al.* (1994) and Appendix A.

The bubbles are released with initial velocity equal to the local flow velocity at random positions which are uniformly distributed over the whole domain. Then the code is run for several large-eddy turnover times in order to achieve a statistically stationary state. Finally, the statistics is accumulated for around 15 large-eddy turnover times τ_0.

2.3. *Bubble's action on the flow in a point-force approximation*

A small bubble rising in a fluid can be viewed as a point-like source of momentum that may either enhance or reduce the kinetic energy of the flow. This modulation is due to a mechanism, whose action is confined to the bubble's nearest region, that supplies the momentum conservation of the overall two-phase system. A δ-forcing is suitable to represent it in the Navier–Stokes equations when the particles are small with respect to all flow scales. As found by Saffman (1973), the effect of small particles on a viscous flow can be taken into account by a multipole distribution of forces. If we now focus on a single sinking particle, the induced velocity in an otherwise still fluid contains two terms: the first decreasing as $1/r$ and the second as $1/r^3$. If the particle is smaller than the Kolmogorov scale, the second contribution is negligible, because the small-scale interactions are dissipated by viscosity. The only effective term that is $O(1/r)$ originates from the δ-forcing in the multipole expansion: therefore the single-particle action can be included in the fluid equation by a δ-*forcing* approximation. This approximation is retained for many bodies, providing that the system is dilute enough. For our two-way coupling simulations, this is the case, see Appendix C.

We report here the main steps that lead to the expression of the coupling term, closely following the procedure of Climent (1996) (see also Maxey *et al.* 1994; Sridhar & Katz 1999; Rightley & Lasheras 2000). We consider a domain $\mathscr{V}$ filled by a fluid of volume $\mathscr{V}_f$ and containing a spherical particle or bubble of volume $\mathscr{V}_p$, thus $\mathscr{V} = \mathscr{V}_f + \mathscr{V}_p$. The flow is bounded by the external surface S_e and the particle surface S_p, see figure 1.

The momentum equation for the fluid in volume $\mathscr{V}_f$ is

$$\int_{\mathscr{V}_f} \rho_f \frac{\mathrm{D}\boldsymbol{u}}{\mathrm{D}t}\,\mathrm{d}\mathscr{V} = \int_{S_e} \boldsymbol{\sigma}\cdot\boldsymbol{n}\,\mathrm{d}S + \int_{S_p} \boldsymbol{\sigma}\cdot\boldsymbol{n}\,\mathrm{d}S + \int_{\mathscr{V}_f} \rho_f \boldsymbol{g}\,\mathrm{d}\mathscr{V}. \tag{2.7}$$
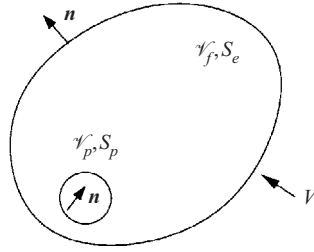
FIGURE 1. A particle of volume $\mathscr{V}_p$ and surface S_p is embedded in a fluid of volume $\mathscr{V}_f$ and external surface S_e. The directions of the outward normals of $\mathscr{V}_f$ are also shown.

Here $\boldsymbol{\sigma}$ is the stress tensor and $\boldsymbol{n}$ is the outward surface normal. The particle equation of motion is

$$\rho_p \mathscr{V}_p \frac{\mathrm{d}\boldsymbol{v}}{\mathrm{d}t} = -\int_{S_p} \boldsymbol{\sigma} \cdot \boldsymbol{n} \, \mathrm{d}S + \rho_p \mathscr{V}_p \boldsymbol{g}. \tag{2.8}$$

The integral of the fluid stress tensor over the particle surface leads to the additional forces of (2.4). Assuming that the flow gradients are constant on the particle volume and using $\mathscr{V} = \mathscr{V}_f + \mathscr{V}_p$, by manipulating (2.7) and (2.8) we obtain

$$\int_{\mathscr{V}} \rho_f \frac{\mathrm{D}\boldsymbol{u}}{\mathrm{D}t} \mathrm{d}\mathscr{V} = \int_{\mathscr{V}} (\nabla \cdot \boldsymbol{\sigma} + \rho_f \boldsymbol{g}) \, \mathrm{d}\mathscr{V}$$
$$+ \int_{\mathscr{V}} \left[\rho_f \left(\frac{\mathrm{D}\boldsymbol{u}}{\mathrm{D}t} - \boldsymbol{g} \right) + \rho_p \left(\boldsymbol{g} - \frac{\mathrm{d}\boldsymbol{v}}{\mathrm{d}t} \right) \right] \mathscr{V}_p \delta(\boldsymbol{x} - \boldsymbol{y}(t)) \mathrm{d}\mathscr{V}, \tag{2.9}$$

where $\boldsymbol{y}(t)$ is the particle's instantaneous location. The equation indicates that the particle's action on the fluid can be represented in the Navier–Stokes equations by the δ-forcing

$$\rho_f \boldsymbol{f}_b(\boldsymbol{x}, t) = \left[\rho_f \left(\frac{\mathrm{D}\boldsymbol{u}}{\mathrm{D}t} - \boldsymbol{g} \right) + \rho_p \left(\boldsymbol{g} - \frac{\mathrm{d}\boldsymbol{v}}{\mathrm{d}t} \right) \right] \mathscr{V}_p \delta(\boldsymbol{x} - \boldsymbol{y}(t)). \tag{2.10}$$

Inserting (2.4) we can also write

$$\rho_f \boldsymbol{f}_b(\boldsymbol{x}, t) = \left[C_D \frac{\pi a^2}{2} \rho_f |\boldsymbol{v} - \boldsymbol{u}|(\boldsymbol{v} - \boldsymbol{u}) - \rho_f \mathscr{V}_p C_M \left(\frac{\mathrm{D}\boldsymbol{u}}{\mathrm{D}t} - \frac{\mathrm{d}\boldsymbol{v}}{\mathrm{d}t} \right) \right.$$
$$\left. + C_L \mathscr{V}_p \rho_f (\boldsymbol{v} - \boldsymbol{u}) \times \boldsymbol{\omega} \right] \delta(\boldsymbol{x} - \boldsymbol{y}(t)). \tag{2.11}$$

Note that in the case of a bubble of small density $\rho_p \ll \rho_f$ the second term on the right-hand side of (2.10) is negligible compared to the first. Thus the δ-forcing of a single bubble is

$$\boldsymbol{f}_b(\boldsymbol{x}, t) = \mathscr{V}_p \left(\frac{\mathrm{D}\boldsymbol{u}}{\mathrm{D}t} - \boldsymbol{g} \right) \delta(\boldsymbol{x} - \boldsymbol{y}(t)). \tag{2.12}$$

The way to implement this forcing on the grid is as follows. It is linearly projected on the eight nearest nodes to the bubble's location, and the total forcing on each node is obtained by summing the contributions of all bubbles according to

$$V \boldsymbol{f}_b(\boldsymbol{x}, t) = \sum_{i \, \mathrm{in} V} \boldsymbol{f}_b^i (1 - \Delta x^i)(1 - \Delta y^i)(1 - \Delta z^i).$$

Here $V = (2\pi/N)^3$ is the grid cell volume, $N = 128$ is the number of grid points in each direction, Δx^i, Δy^i, Δz^i are the distances, normalized by the mesh size, of bubble i, placed between the grid points at $y_i(t)$, from the node x, and the index i counts the bubbles in V. In this method only the closest grid points to the particle position are taken into account. Another way of including the two-way interactions through the distribution of the backreaction on a larger envelope centred at the particle position is discussed in Maxey et al. (1997).

For turbulent flow the point-force approach is appropriate if the particle dimension is much smaller than the Kolmogorov scale η, i.e. $a/\eta < 1$ (see e.g. Maxey & Riley 1983). The largest radii we use in our simulations are of the order of η. On first sight this may seem dangerously close to the borderline of applicability of the point-force approximation. However, the transition from the viscous subrange to the inertial subrange only occurs at a scale 10η (see e.g. Monin & Yaglom 1975). Therefore, the bubbles in our scheme do not see any turbulent fluctuation around them up to a scale 10 times as large as their radius, and with a point-force approximation one is on the safe side. This is also demonstrated by the following estimate. When a is becoming larger than η, Faxén terms should be taken into account (see Maxey & Riley 1983). If we estimate for instance the error incurred by neglecting Faxén corrections on the drag force: $(-1/\tau_b)(v - u - \frac{1}{6}a^2\nabla^2 u|_{y(t)})$ within our code, we measure relative errors of the order of 1%, which is tolerable.

We remark that the implementation of two-way coupling leads to some restrictions on the bubble regimes achievable through numerical calculations. The fluid velocity u required in the integration of (2.6) is 'un-perturbed', i.e. it is the velocity of the flow unmodified by the bubble. According to Saffman (1973) the error incurred in the approximation of this velocity by the perturbed one is the Stokeslet centred at the particle's position, and is of order $a/\Delta x$, where Δx is the grid space. The constraint is therefore: $a \ll \Delta x$. The error is reduced when: (i) the number of bubbles in the simulation is larger, because in that way the relative influence of each bubble forcing on a grid node is smaller; (ii) a higher-order interpolation scheme for the fluid velocity at the position of the bubble is employed, because nodes further away are involved and the perturbation of the bubble itself is partially filtered.

The quality of the point-force approximation in the forcing is checked in Appendix B by comparing the dynamics of active and passive bubbles.

3. One-way coupling approximation

3.1. *Bubble accumulation in vortices*

In this section we restrict ourselves to one-way coupling, i.e. the bubble backreaction on the flow is neglected. This type of simulations correctly reflects the experimentally observed bubble accumulation in vortices, see e.g. Wang & Maxey (1993a), Maxey et al. (1994) and Sene, Hunt & Thomas (1994). In table 1 of Mazzitelli et al. (2003) we quantified the bubble accumulation for the present simulation, by comparing the mean enstrophy at the bubble position with the total mean enstrophy. This ratio is between 1.6 and 2.2, depending on the bubble size. Once the lift force is turned off, it further increases, indicating that with lift present the bubbles on average do not sit close to the very centres of the vortices. In fact, we could confirm the speculation of Spelt & Biesheuvel (1997) that the lift force strongly contributes to push them to the downflow side of the vortices.

Fluid zone	Eddy (%)	Shear (%)	Streaming (%)	Convergence (%)
W & H DNS	13	6	25	4
Present DNS (1-way)	11	6	26	6
Present DNS (2-way)	10	7	25	3

TABLE 2. Volume fractions occupied by eddy, shear, streaming and convergence zones, in Wray & Hunt (1990) (first row), in the present simulation (second row), and in the present simulation with two-way coupling (third row). For our simulation $v_T = 2v_k$ and $\tau_b = \tau_k/10$, and the lift force is included.

The dimensionless parameter characterizing the interaction of a bubble with a vortex is

$$\beta = \frac{u_0}{v_T} = \frac{3u_0\nu}{ga^2}. \tag{3.1}$$

It gives an indication of which structures can trap the bubble (Sene *et al.* 1994). When $\beta \gg 1$ (i.e. a small bubble) trapping occurs in all structures, including the smallest ones, whereas $\beta \ll 1$ (i.e. large bubble) indicates that the bubble moves fast through the flow, essentially without any interaction. We will extensively use the parameter β throughout this paper.

3.2. *Bubble distribution between different flow zones*

How to further characterize the zones in the flow where the bubbles go? Flow regions with distinct characteristics can be classified according to Wray & Hunt (1990) who define four types of structures: *eddies*, where the vorticity is high and the flow displays a circulating pattern; *shear* zones, with yet higher vorticity but no rotation; *convergence* zones, in which the velocity lines converge or diverge; and *streaming* zones, corresponding to high-velocity regions without particular strain or rotation. The four different zones can be distinguished by measuring three quantities: the fluid velocity $\boldsymbol{u}$, the shear stress Π, defined as $\Pi = (\partial u_i/\partial x_j)(\partial u_j/\partial x_i)$ and the flow pressure p, that is connected to the shear stress by the Poisson equation $\Delta p = -\Pi$. The local values are then compared with their r.m.s. values: Π_{rms}, p_{rms}, and u_0. This procedure leads to the following classification:

(*a*) eddy zones: $\Pi < -\Pi_{rms}/2$ and $p < -p_{rms}/2$,

(*b*) shear zones: $\Pi < -\Pi_{rms}/2$ and $-p_{rms}/2 < p < p_{rms}$,

(*c*) streaming zones: $|\Pi| < \Pi_{rms}/2$ and $|\boldsymbol{u}| > u_0$,

(*d*) convergence zones: $\Pi > \Pi_{rms}$ and $p > p_{rms}$.

Note that different regions do not overlap and that there are regions in the computational domain which are in none of these zones. In table 2 the volume percentage occupied by the various zones obtained from DNS by Wray & Hunt (1990) is compared to the percentage in the present simulation. The agreement is extremely good. The last line of the table shows results in the two-way coupling case.

We now investigate how bubbles are distributed in these fluid regions. In figure 2 the fraction of bubbles located in the four zones, normalized by the region volume fraction (see table 2), is plotted as a function of τ_b/τ_k. The rise velocity is fixed: $v_T = v_k$. The ratios are evaluated by averaging over 2 large-eddy turnover times.

The results show that there is clustering in high-vorticity regions and preferentially in eddies compared to shear zones. The strongest effect occurs when $\tau_b \simeq \tau_k$ with
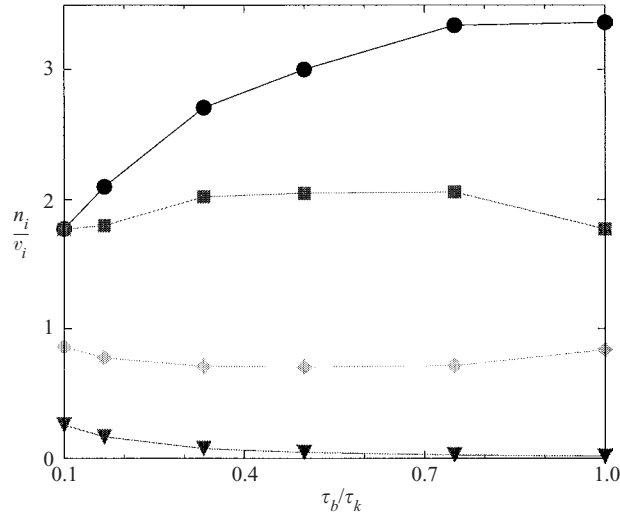
FIGURE 2. Fraction of the number of bubbles located in a particular zone of fluid n_i, normalized by the volume fraction of this zone v_i, as a function of the ratio τ_b/τ_k, for fixed $v_T = v_k$. The various symbols refer to zones: eddy (circles), shear (squares), streaming (diamonds) and convergence (triangles).

three times larger concentration in eddy zones than would be measured in the case of a uniform bubble distribution. The phenomenon monotonically decreases for smaller τ_b, but it is still present even for the smallest time ratio analysed ($\tau_b/\tau_k = 1/10$). Note that this result is important in view of simulations with two-way coupling that we carry out in this regime. The other ratios presented in figure 2 show less dependence on the bubble response time. We observe that convergence zones are devoid of bubbles.

These results on the bubble distribution in the flow can be compared to the analysis of Spelt & Biesheuvel (1997), who study bubble motion in homogeneous and isotropic turbulence obtained by kinematic simulations, rather than by full Navier–Stokes dynamics. Nevertheless, the results agree pretty well, both from a qualitative and a quantitative point of view.

4. Two-way coupling

In this section we analyse how the bubbles modify the turbulent flow (two-way coupling). Therefore, the coupling f_b of microbubbles to the flow in (2.1) is no longer neglected. The void fraction is $\alpha = 1.6\%$ and the bubble response time $\tau_b = \tau_k/10$, thus the bubble radius $a = \sqrt{6\nu\tau_b}$ is kept constant. We scan different bubble regimes by varying the rise velocity in quiescent fluid $v_T = 2g\tau_b$. The ratio of the bubble radius to the Kolmogorov scale is $a/\eta \sim 0.8$. Moreover, bubble–bubble direct interactions are neglected, as we consider low void fractions. Quantitative information on the bubble clustering encountered in our simulation is given in Appendix C.

The range of parameters analysed throughout the numerical simulations presented here corresponds to microbubbles of diameter $d \sim 120$–$250\,\mu\text{m}$ in clean water ($\nu = 10^{-2}\,\text{cm}^2\,\text{s}^{-1}$ and $g = 981\,\text{cm}\,\text{s}^{-2}$). The rise velocity $v_T = gd^2/(12\nu)$ of such bubbles is $1 - 5\,\text{cm}\,\text{s}^{-1}$, which agrees with the experimental observations, see figure 7.3 of Clift, Grace & Weber (1978).

4.1. *Modification of the energy spectrum*

The effect of bubbles on turbulence has been taken into account by adding an extra forcing-like term to the Navier–Stokes equations (2.1). When transforming to the wavenumber space and, in particular, to the spectral form of the energy transfer equation, we obtain the following expression:

$$\frac{\partial}{\partial t} E(k) = T(k) - 2\nu k^2 E(k) + F_L(k) + F_b(k). \tag{4.1}$$

Here $F_L(k)$ is the production due to the large-scale forcing and $F_b(k)$ the forcing contribution of the bubbles. $E(k)$ is the energy spectrum

$$E(k) = \frac{1}{2} \sum_{k<|\mathbf{k}|<k+dk} u_i^*(\mathbf{k}) u_i(\mathbf{k}), \quad i = x, y, z, \tag{4.2}$$

i.e. it is the energy contained in a shell of radius k and thickness dk. Multiplying $E(k)$ with $2\nu k^2$, we obtain the so-called dissipation spectrum

$$D(k) = 2\nu k^2 E(k). \tag{4.3}$$

$T(k)$ is the energy transfer to wavenumber k:

$$T(k) = \sum_{k<|\mathbf{k}|<k+dk} T(\mathbf{k}), \tag{4.4}$$

where

$$T(\mathbf{k}) = \mathrm{Im}\left(k_j u_l^*(\mathbf{k}) \sum_{\mathbf{k}'} u_j(\mathbf{k} - \mathbf{k}') u_l(\mathbf{k}') \right). \tag{4.5}$$

After summing on all k, taking into account that

$$\sum_k T(k) = 0, \tag{4.6}$$

and defining

$$\epsilon = \sum_k D(k), \quad F_L = \sum_k F_L(k), \quad F_b = \sum_k F_b(k), \tag{4.7}$$

one has

$$-\epsilon + F_L + F_b = 0 \tag{4.8}$$

in the stationary state. We can establish whether the bubbles enhance or reduce the turbulent energy by computing the fluid viscous dissipation in wavenumber space $D(k) = 2\nu k^2 E(k)$ and its integrated value ϵ. If the fluid dissipation ϵ is smaller than F_L, which equals 1 by definition, see equation (2.3) and table 1, the bubbles attenuate the energy supplied at large scales ($F_b < 0$), otherwise, if $\epsilon > F_L$, the bubbles force the flow ($F_b > 0$), so that extra viscous dissipation is necessary to maintain a stationary state.

We have carried out such analysis in Mazzitelli *et al.* (2003), with the help of the numerical simulation described here. The simulations show that the bubble forcing leads to an energy enhancement at small scales, but an energy reduction at large length scales, see figure 3. The overall effect is a reduction of the total energy dissipation, see figure 4. The origin of this effect lies in the lift force which makes bubbles cluster in downflow regions. These bubble clouds locally transfer momentum upwards, thus attenuating the vertical fluid velocity fluctuations. Similar effects have
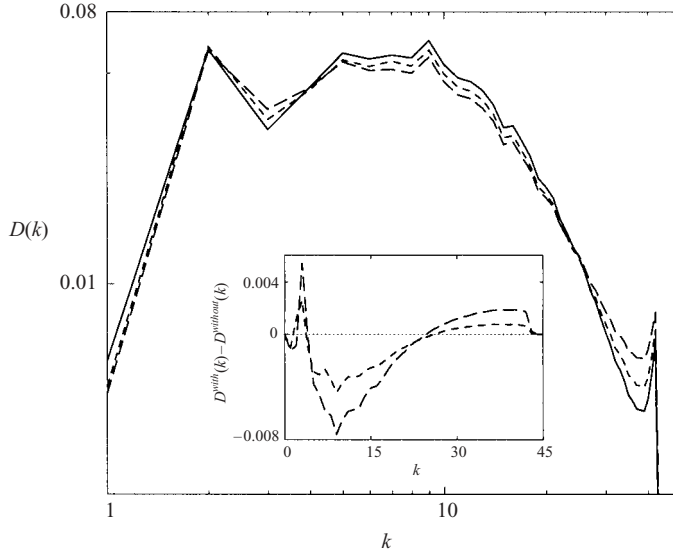
FIGURE 3. Dissipative spectrum for one-phase flow (solid line) and for two cases of active bubbles coupled to the turbulence: $v_T = 2v_k$ (dashed line), and $v_T = 4v_k$ (long dashed line). In both cases $\tau_b = \tau_k/10$. The inset shows the difference between the two-phase spectrum and the one-phase spectrum.
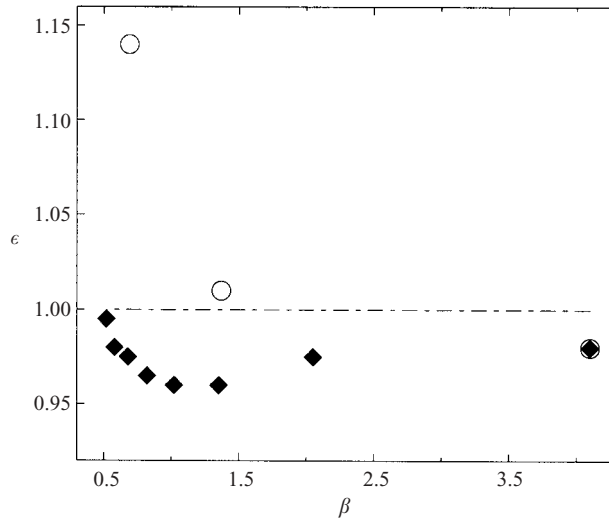

FIGURE 4. Total flow dissipation in simulations with active bubbles as a function of the ratio $\beta = u_0/v_T$. The bubble response time is in all cases $\tau_b = \tau_k/10$. The filled symbols (diamonds) indicate simulations with lift force, whereas the open symbols (circles) refer to simulations without lift. The straight line indicates the one-phase flow value: $\epsilon = 1$.

been experimentally found by Sridhar & Katz (1999), when analysing microbubble distortion of vortex rings.

The reduction of the total energy dissipation in turbulent flow is indeed remarkable. In flow which is initially at rest ($Re_\lambda = 0$, $\epsilon = 0$) and then driven only by bubbles (i.e. $f_L = 0$, 'pseudoturbulence', see e.g. van Wijngaarden 1998; Climent & Magnaudet
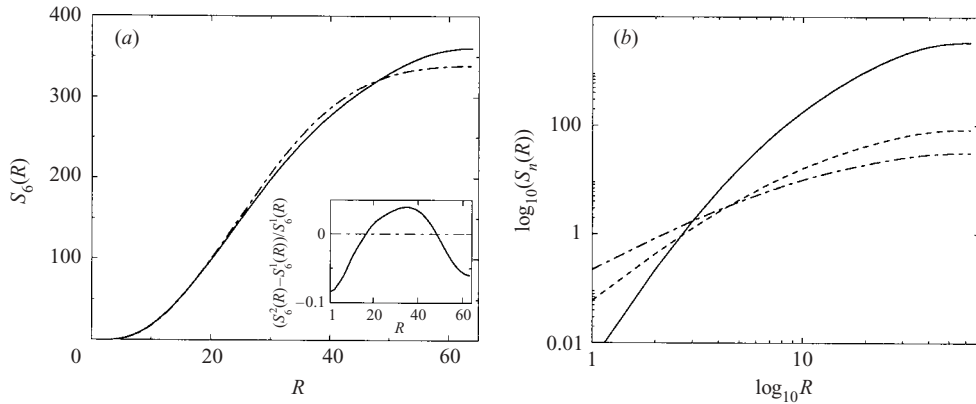
FIGURE 5. (a) Structure functions $S_6(R)$ vs. R, for single- (solid line) and two-phase flow (dot-dashed line) with $v_T = 2v_k$, $\tau_b = \tau_k/10$. In the inset the relative difference $(S_6^{2way}(R) - S_6^{1way}(R))/S_6^{1way}(R)$ is presented. The plot shows that the intensity modulation is not uniform on all scales as we have already found when looking at the spectral energy dissipation, see figure 3. (b) Structure functions $S_n(R)$ vs. R, on logarithmic scale for $n = 2$ (dot-dashed line), $n = 3$ (dashed line), and $n = 6$ (solid line). All plots refer to the two-way coupling regime. Due to the low flow Reynolds number no scaling in R is detectable.

1999), one of course has an increase of the energy dissipation to $\epsilon = F_b$, and also Re_λ will become larger than zero. Note that in between that case with initially $Re_\lambda = 0$ (leading to an enhancement of ϵ) and the case studied here with initially $Re_\lambda = 62$ (leading to a reduction of ϵ) there must be some Taylor–Reynolds number for which the energy dissipation rate ϵ remains unmodified.

4.2. *Modification of the velocity structure functions*

In this subsection we study how the two-way coupling modifies the scaling properties of the turbulence in r-space. To this end we plot longitudinal velocity structure functions:

$$S_n(R) = \langle |(u(x + R) - u(x)) \cdot \hat{R}|^n \rangle \qquad (4.9)$$

(where R is the distance vector, $R = |R|$) of various order n and compare the behaviour with that for the single-phase flow case. From our results on the spectra in the previous subsection one would expect that in the two-way coupling case (i) large scales $L > r > 10\eta$ have less energy than in the one-way coupling case and (ii) small scales $r \approx \eta$ have more energy. (iii) In addition, at least for the second-order structure function which behaves like $S_2(R) = \epsilon R^2/(15\nu)$ for $r \ll \eta$, for very small scales there should be less intensity in the two-phase coupling case, as the total energy dissipation rate ϵ is less for two-way coupling.

In figure 5(a) the structure functions $S_6(R)$ are plotted, both for single- and two-phase flow. The graphs, on a linear scale, show the modulation in the intensity due to the two-way coupling. The modification is consistent with above expectations (i)–(iii). However, here we must caution that other structure functions show different features. In particular, this holds for the second-order structure function which is connected to the energy spectrum through a Fourier-transformation. We suspect that deviations from expectations (i)–(iii) originate from finite size effects. Indeed, for the limited Taylor–Reynolds numbers in our numerical simulations the scaling regime is very small and as shown in Lohse & Müller-Groeling (1995, 1996), finite size effects in the relation between the structure function and the energy spectrum can be considerable.
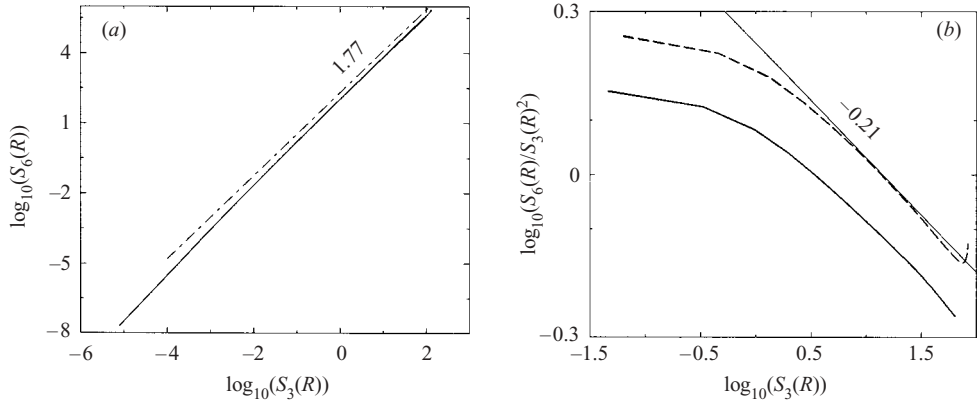
FIGURE 6. (a) ESS plot of $S_6(R)$ vs. $S_3(R)$, for one-way coupling and for two-way coupling, with $v_T = 2v_k$, $\tau_b = \tau_k/10$, including the lift force (solid line). The two curves overlap on the logarithmic scale. The straight dash-dotted line indicates the scaling behaviour in homogeneous and isotropic turbulence. (b) Compensated ESS plot, presenting $S_6(R)/S_3^2(R)$ vs. $S_3(R)$, for one-way coupling (dashed) and two-way coupling, with $v_T = 2v_k$, $\tau_b = \tau_k/10$, including the lift force (solid). Through the compensation the deviations from the non-intermittent case (slope 0 instead of slope -0.21 as here) become particularly visible (Grossmann *et al.* 1997).

Note also that, in terms of the scale-dependent time scale, the effect on the statistics on the very large scales is greatest.

Also, owing to the low flow Reynolds number, the structure functions do not display any power law when plotted versus the scale R (see figure 5(b)). However, very often these structure functions still show scaling when plotted against each other. This feature is called extended self-similarity (ESS, Benzi *et al.* 1993).

In figure 6(a), we present the ESS plots of $S_6(R)$ versus $S_3(R)$, again for single- and two-phase flow, and scaling is indeed recovered. However, this type of plot is not precise enough to show a possible difference in scaling between the one-way and two-way coupling cases. Therefore we also plot the so-called compensated ESS plot (Grossmann, Lohse & Reeh 1997b) see figure 6(b). We detect good agreement of the two-way coupling structure function scaling with the scaling displayed by structure functions in homogeneous and isotropic turbulence. Therefore we infer that the two-way coupling does not modify the ESS scaling exponents within our numerical accuracy, i.e. bubbly turbulence displays the same amount of intermittency as standard turbulence. This result resembles the findings of Benzi *et al.* (1996) in which a remarkable universality of the ESS scaling exponents for various types of flow (three-dimensional homogeneous turbulence, thermal convection, MHD turbulence) has been found. Apparently, bubbly turbulence belongs to the same universality class.

4.3. *Modification of global quantities*

We now report the results of our two-way coupling simulations for several global quantities in order to further clarify how the bubble forcing modifies the turbulence.

We recall that $a/\eta \simeq 0.8$. Small bubble dimensions with respect to all flow scales are required for the application of the point-force approximation (see §2.3). The value of the bubble rise velocity $v_T = 2g\tau_b$ is changed in different runs by varying the intensity of the gravity force, from 0 to $40v_k/\tau_k$. The total number of bubbles is $N_{tot} = 144\,000$.

Various physical observables are shown in table 3. The brackets $\langle \cdot \rangle$ indicate temporal averages. $\langle \Omega \rangle_b/\Omega$ is the time-averaged enstrophy at the bubble location

$\tau_b = \tau_k/10$	$v_T = 0$	$v_T = v_k$	$v_T = 2v_k$	$v_T = 3v_k$	$v_T = 4v_k$	$v_T = 5v_k$	$v_T = 6v_k$	$v_T = 7v_k$	$v_T = 8v_k$
radius (μm)	–	62	78	89	98	106	112	118	124
$\beta = u_0/v_T$	∞	4.1	2.05	1.35	1.02	0.82	0.68	0.58	0.52
ϵ	0.99 ± 0.02	0.98 ± 0.04	0.975 ± 0.03	0.96 ± 0.04	0.96 ± 0.03	0.965 ± 0.03	0.975 ± 0.03	0.98 ± 0.02	0.995 ± 0.03
$3u_0^2/2$	2.09 ± 0.04	2.14 ± 0.045	2.11 ± 0.05	2.07 ± 0.05	2.09 ± 0.05	2.12 ± 0.05	2.01 ± 0.045	2.09 ± 0.06	2.14 ± 0.05
$\langle\Omega\rangle_b/\Omega$	1.68 ± 0.04	1.57 ± 0.05	1.39 ± 0.05	1.29 ± 0.04	1.22 ± 0.03	1.165 ± 0.02	1.12 ± 0.02	1.10 ± 0.015	1.09 ± 0.01
$(\langle v_z\rangle - v_T)/v_T$	0	-0.065	-0.04	-0.04	-0.028	-0.02	-0.009	-0.0075	-0.004
N_-/N_{tot}	$0.5 \pm 9 \times 10^{-3}$	$0.503 \pm 7 \times 10^{-3}$	$0.513 \pm 9 \times 10^{-3}$	$0.513 \pm 7 \times 10^{-3}$	$0.511 \pm 8 \times 10^{-3}$	$0.511 \pm 7 \times 10^{-3}$	0.504 ± 0.01	0.500 ± 0.01	$0.504 \pm 8 \times 10^{-3}$
Re_λ	61 ± 2	63 ± 3	62 ± 2	62 ± 3	62 ± 2	64 ± 3	63 ± 3	62 ± 2	63 ± 3
Re_λ^x	59 ± 6	66 ± 6	63 ± 5	63 ± 7	62 ± 5	65 ± 6	66 ± 6	65 ± 5	69 ± 5
Re_λ^y	63 ± 4	65 ± 6	68 ± 5	65 ± 6	67 ± 4	66 ± 8	67 ± 7	62 ± 6	66 ± 5
Re_λ^z	62 ± 5	58 ± 4	56 ± 3	57 ± 5	56 ± 5	59 ± 5	54 ± 3	58 ± 6	56 ± 4
$\langle u_x^2\rangle$	1.23 ± 0.09	1.38 ± 0.08	1.29 ± 0.09	1.3 ± 0.1	1.3 ± 0.1	1.3 ± 0.1	1.35 ± 0.1	1.3 ± 0.1	1.4 ± 0.07
$\langle u_y^2\rangle$	1.30 ± 0.08	1.3 ± 0.1	1.39 ± 0.08	1.3 ± 0.1	1.36 ± 0.07	1.35 ± 0.1	1.35 ± 0.1	1.3 ± 0.1	1.36 ± 0.09
$\langle u_z^2\rangle$	1.29 ± 0.08	1.21 ± 0.09	1.17 ± 0.05	1.17 ± 0.08	1.17 ± 0.09	1.19 ± 0.09	1.13 ± 0.07	1.2 ± 0.1	1.17 ± 0.08

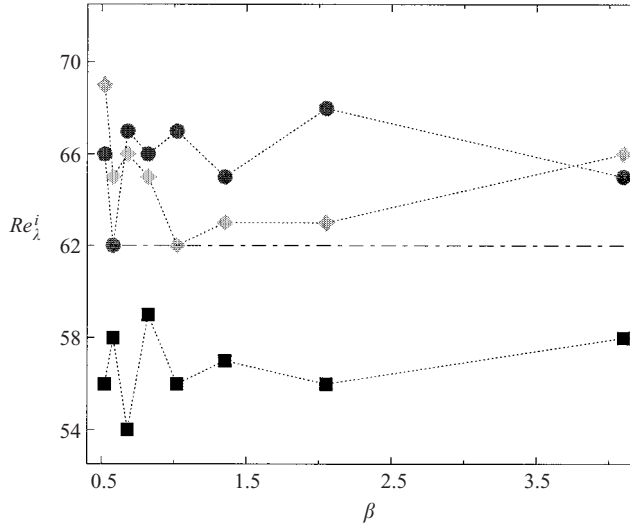TABLE 3. Bubble and fluid observables in simulations with two-way coupling.

FIGURE 7. Taylor–Reynolds number as a function of $\beta = u_0/v_T$ in the three directions: x (diamonds), y (circles), and z (squares). The straight line indicates the one-phase flow value $Re_\lambda = 62$.

normalized with respect to the average fluid enstrophy and N_-/N_{tot} is the fraction of bubbles sampling downflow zones. The Taylor–Reynolds number in the *ith* direction is computed according to

$$Re_\lambda^i = \sqrt{\frac{\langle u_i^2 \rangle}{\langle (\partial_i u_i)^2 \rangle}} \frac{\sqrt{\langle u_i^2 \rangle}}{\nu} \quad \text{(no sum over } i\text{)}.$$

The β-dependences of these unidimensional Taylor–Reynolds numbers are plotted in figure 7. Like the values of the fluid r.m.s. velocity fluctuations in table 3, the figure demonstrates that the bubbles act anisotropically, i.e. they preferentially attenuate the vertical (z) velocity fluctuation. Indeed, Re_λ^z is smaller than in the single-phase flow case (where $Re_\lambda = 62$), thus revealing a slightly lower turbulence intensity in this direction. On the other hand, the Taylor–Reynolds numbers in the x- and y-directions are slightly enhanced when compared to the one-phase flow. This is due to the fluid incompressibility. Anisotropy is also detected in the fluid velocity gradients $\langle (\partial_i u_i)^2 \rangle$ (not reported in the table), which are larger in the z-direction than in the other two. However, the total Taylor–Reynolds number is always consistent, within statistical fluctuations, with the single-phase Reynolds number $Re_\lambda = 62$ and shows no pronounced β-dependence.

The result is very different for the mean enstrophy at the bubble position compared to the total mean enstrophy and the bubble rise velocity, see figures 8 and 9. In the large-β case, corresponding to a small bubble velocity scale v_T (small bubbles or small gravity; note that an increase of β can also be achieved by increasing u_0, i.e. stronger turbulence), the trapping of the bubbles in the vortices is more pronounced, leading to a relatively large $\langle \Omega \rangle_b / \Omega$ and a reduction of the bubble rise velocity in the turbulence. On the other hand, in the small-β case (large v_T, a, or g, or small u_0), the bubbles hardly feel the vortices: correspondingly, they are hardly trapped by the vortices and their rise velocity in the turbulent flow is basically the same as in still water.
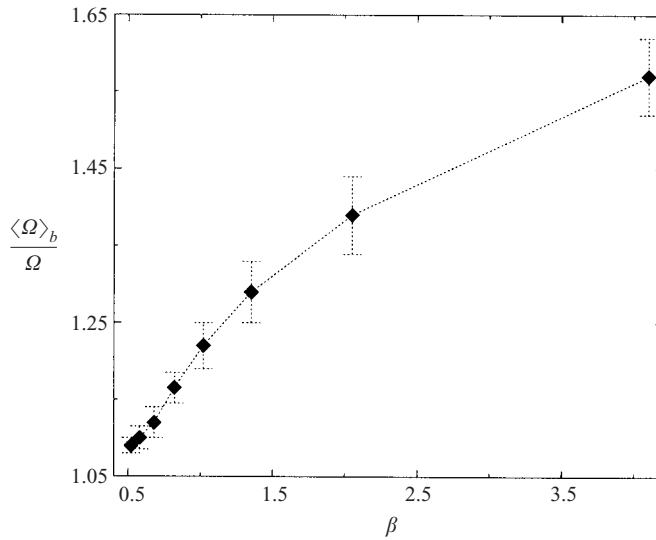
FIGURE 8. Enstrophy at the bubble location normalized by the average flow enstrophy, given as a function of $\beta = u_0/v_T$.
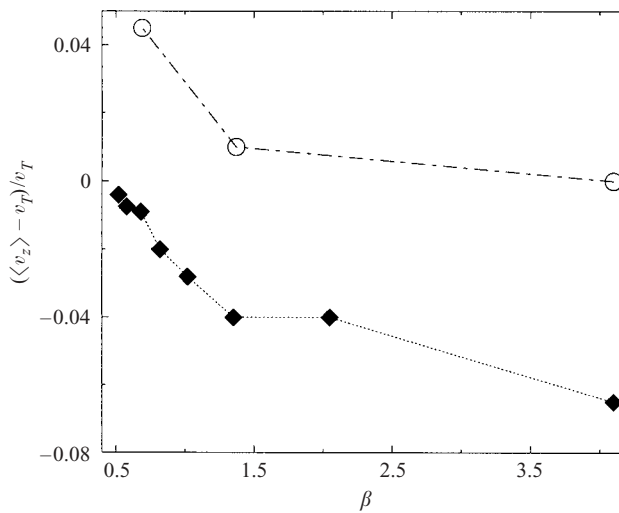

FIGURE 9. Relative reduction of the bubble rise velocity in turbulence compared to the rise velocity v_T for still water, $(\langle v_z \rangle - v_T)/v_T$. The filled symbols correspond to our two-way coupling simulation with lift (§4), the open symbols to a simulation in which the lift force had artificially been set to zero in order to demonstrate its importance (§5).

For two-way coupling the consequence of the bubble trapping in the vortices is the smoothing of the velocity fluctuations. Since bubbles are caught by structures with velocity of the order of v_T, the maximum attenuation of kinetic energy occurs when $v_T \simeq u_0$, or, in other words, $\beta \simeq 1$. It is precisely in this regime that bubbles suppress the large-scale eddies in which most of the flow energy is contained, see figure 4.

$\tau_b = \tau_k/10$	$v_T = v_k$	$v_T = 3v_k$	$v_T = 6v_k$
radius (μm)	62	89	112
$\beta = u_0/v_T$	4.1	1.37	0.69
ϵ	0.98 ± 0.03	1.01 ± 0.03	1.14 ± 0.035
$3u_0^2/2$	2.11 ± 0.04	2.11 ± 0.06	2.13 ± 0.05
$\langle \Omega \rangle_b/\Omega$	1.57 ± 0.04	1.25 ± 0.03	1.12 ± 0.02
$(\langle v_z \rangle - v_T)/v_T$	0	$+0.01$	$+0.045$
N_-/N_{tot}	$0.495 \pm 7 \times 10^{-3}$	$0.483 \pm 7 \times 10^{-3}$	$0.467 \pm 8 \times 10^{-3}$
Re_λ	62 ± 2	61 ± 3	60 ± 2
Re_λ^x	59 ± 5	59 ± 6	62 ± 7
Re_λ^y	62 ± 4	65 ± 6	61 ± 5
Re_λ^z	63 ± 4	60 ± 7	56 ± 4
$\langle u_x^2 \rangle$	1.23 ± 0.09	1.2 ± 0.1	1.3 ± 0.1
$\langle u_y^2 \rangle$	1.3 ± 0.07	1.35 ± 0.1	1.3 ± 0.1
$\langle u_z^2 \rangle$	1.32 ± 0.07	1.2 ± 0.1	1.25 ± 0.07

TABLE 4. Bubble and fluid observables in simulations with two-way coupling and without lift force in the bubble equation of motion.

5. Flow modification in the absence of the lift

The best way to highlight the importance of the lift force on the dynamics of turbulent bubbly flow is to turn off this force in the numerical simulations. Therefore, we perform numerical simulations by calculating the bubble trajectories without the lift force in (2.6). The same bubble–flow quantities as in §4 are measured and shown in table 4. Note that two-way coupling is still applied. The result is that many observables become qualitatively different in this simulation, mainly because now fewer bubbles are pushed into the downflow region as the lift is set to zero.

First we comment on the quantities that describe the dispersed phase. The average enstrophy at the bubble locations normalized by the mean flow enstrophy, $\langle \Omega \rangle_b/\Omega$, reaches the same values as in the corresponding simulations with lift force, thus indicating that bubbles are accumulating in vortex structures of equal intensity. In Mazzitelli *et al.* (2003) we measured lower ratios in the case with lift force than in the case without, for simulations with only one-way coupling. We infer that in the two-way coupling case the bubble forcing introduces velocity gradients that enhance the local vorticity.

Sridhar & Katz (1999) discuss the effect of bubble buoyancy and of the pressure gradient terms (see (2.12)) on vortex rings. The gravity on the bubble acts to displace the vortex core, whereas pressure gradient reduces the area of the vortex and therefore increases the local vorticity. It is reasonable to expect a similar effect in the numerical simulations, where bubbles smooth the vertical fluid velocity because of the buoyant force, but, at the same time, force the flow through the pressure gradient term (fluid acceleration term in (2.12)), which points towards the vortex centres. The pressure gradient term is larger in simulations where lift force is included, because bubbles are located further from the vortex cores than when lift forces are not considered. The result is that the increase of the local vorticity is larger when including lift forces than when excluding them and this effect apparently compensates for the enstrophy difference that we had measured in one-way coupling runs.

The ratio $N_-/N_{tot} < 0.5$ shows that most bubbles are now sampling fluid regions in which the flow velocity is opposite to gravity. As a consequence a small increase
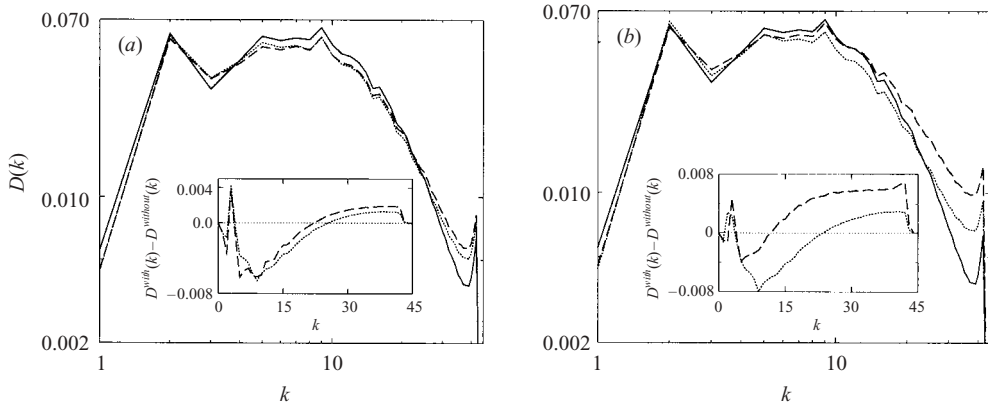
FIGURE 10. Dissipation spectra in two regimes: (*a*) $v_T = 3v_k$ and (*b*) $v_T = 6v_k$. The curves represent the flow with one-way coupling (solid line), two-way coupling with lift effect (dotted line) and without lift (dashed line). The insets show the difference between the two-way and the one-way coupling spectrum, in a simulation with lift (dotted line) and without (dashed line).

of the average rise velocity $\langle v_z \rangle$ compared to the terminal speed v_T is detected. We explain this phenomenon by considering the indirect bubble–bubble interactions, that occur via the underlying flow (remember that direct interactions are neglected). In fact, without lift force the clustering in downflow zones is reduced (see table 1 of Mazzitelli *et al.* 2003). Thus, the bubble local momentum transfer is more likely to produce vertical fluid velocity fluctuations in the positive z-direction, which are experienced by nearby bubbles.

Second, we focus on the flow modification. Even though the bubble forcing is anisotropic, the Taylor–Reynolds numbers and the fluid velocity fluctuations are the same in all directions x, y, and z. This is in strong contrast to the simulation with lift (previous section and in particular figure 7). The reason again is that without lift the bubbles are no longer preferentially in downflow regions.

The most relevant feature of the two-way coupling simulation without lift is the increase of the energy dissipation in comparison with one-phase turbulence, see figure 4 (open symbols). This increase means a qualitative difference to the simulations with lift: the bubbles are now acting as a source of turbulent energy, cf. (4.8).

The modification of the dissipative spectrum by the bubble forcing is shown in figure 10. We compare the spectra in simulations with and without lift force, and the single-phase flow spectrum. The bubble rise velocities considered are $v_T = 3v_k$ and $v_T = 6v_k$. On increasing the rise speed the attenuation of the large-scale energy with respect to one-phase turbulence is smaller and the effect of bubbles mimics an energy source at almost all scales.

In conclusion, the comparison of these simulations and those of §4 clearly demonstrates the importance of including all forces in the equation for the bubble dynamics, including the lift: neglecting some of the forces may lead to erroneous and even qualitatively different results.

6. Importance of clustering on two-way interactions

In this section we will demonstrate the crucial role of bubble clustering for the observed spectral modification. Again, the best way to demonstrate the importance is

to turn off the clustering effect. We do so by fixing the bubbles at random positions in space. Note that the bubbles still force the flow (two-way coupling).

6.1. *Comparison between bubble-laden and heavy-particle-laden turbulence*

For dispersed multiphase flow with heavy particles in the dispersed phase the energy dissipation reduction can reach rather high values, up to the 60% compared to the single-phase spectrum (e.g. see Boivin *et al.* 1998). In the bubble-laden case the maximum attenuation of the fluid energy we find is of the order of 4% (for a void fraction $\alpha \simeq 1.6\%$). The main difference between bubble-laden and particle-laden turbulence is that bubbles have negligible density. Then all the system inertia is carried by the fluid phase. Particles, on the other hand, may possess much more inertia than the flow, so that the fluid has to supply kinetic energy in order to accelerate them. Accordingly, the mechanism of energy attenuation is substantially different in the case of particle flow than bubbly flow. In dispersed particle flow it is linked to the work done by the fluid to impose acceleration, whereas in dispersed bubbly flow it is connected to the bubble tendency to accumulate in particular flow regions and to their local action in these zones.

6.2. *Comparison between bubble-laden and small-particle-laden turbulence*

For particles of small inertia, $\tau_p = d^2(\rho_p/\rho_f)/(18\nu) \ll \tau_k$, yet heavier than the fluid ($\rho_p \gg \rho_f$), the situation is again different. As pointed out by Saffman (1962) and Druzhinin (2001), the main effect of the particles now is to increase the fluid density and, therefore, to reduce the effective kinematic viscosity. As a consequence the turbulence is enhanced by two-way coupling.

Further insight is gained by considering the particle–fluid coupling equation (2.10). This expression has two terms on the right-hand side and, depending on the density ratio ρ_p/ρ_f, one may be more relevant than the other. As already stressed, for bubbles the first term is dominant, whereas for particles of high density it is the second. Moreover, in the latter case, when adding the condition $\tau_p/\tau_k \ll 1$, the time evolution is dominated by the Stokes drag force and the gravity. It follows that, at zero order in the ratio τ_p/τ_k, the particle acceleration is equal to the local fluid acceleration, i.e. $d\boldsymbol{v}/dt \simeq D\boldsymbol{U}/Dt$. Therefore, from (2.10) we establish that bubbles and particles have opposite action on the flow, and this result holds also for non-gravity terms.

For the microparticle ($\tau_p \ll \tau_k$) regime Druzhinin (2001) derived an analytical expression for the microparticle forcing term, assuming uniform particle concentration. It is found that, in a first approximation, particles behave as a source of turbulent energy.

6.3. *Analytical estimate of spectral modification*

We can carry out the analogous calculation of Druzhinin (2001) in the case of microbubbles. The starting point is the Navier–Stokes equation with two-way coupling, which we rewrite as

$$\frac{D\boldsymbol{u}}{Dt} = -\nabla p + \nu \Delta \boldsymbol{u} + \alpha(\boldsymbol{x}, t)\left(\frac{D\boldsymbol{u}}{Dt} - \boldsymbol{g}\right), \qquad (6.1)$$

neglecting the large-scale forcing. Here $\alpha(\boldsymbol{x}, t)$ is the local bubble concentration and it contains all the information on the bubble evolution. We now assume uniform and constant bubble distribution, i.e. $\alpha(\boldsymbol{x}, t) = \alpha$, independent of $\boldsymbol{x}$ and t. As a consequence, the two-way coupling term (2.12) loses the details of the bubble motion. Therefore it is not necessary to specify the bubble equation of motion and in particular whether the lift force is switched on or off.

After transforming to wavenumber space, (6.1) becomes

$$(1 - \alpha)\frac{\mathrm{D}u_j(\boldsymbol{k})}{\mathrm{D}t} = -\mathrm{i}k_j P(\boldsymbol{k}) - \nu k^2 u_j(\boldsymbol{k}) - \alpha g \delta_{jz}\delta_{|\boldsymbol{k}|,0}, \quad j = x, y, z. \tag{6.2}$$

Here $\mathrm{D}u_j(\boldsymbol{k})/\mathrm{D}t$ is the Fourier transform of the total material derivative of $\boldsymbol{u}$ and $P(\boldsymbol{k})$ is the Fourier transform of the pressure, $p(\boldsymbol{x})$. Our goal is to compute the bubble term $F_b(k)$ of the energy transfer equation (4.1), defined according to (see (4.4))

$$F_b(k) = \sum_{k < |\boldsymbol{k}| < k + dk} F_b(\boldsymbol{k}),$$

where $F_b(\boldsymbol{k})$ now is

$$F_b(\boldsymbol{k}) = \alpha \, \mathrm{Re}\left\{ u_j^*(\boldsymbol{k})\left(\frac{\mathrm{D}u_j(\boldsymbol{k})}{\mathrm{D}t} - g\delta_{jz}\delta_{|\boldsymbol{k}|0}\right)\right\}. \tag{6.3}$$

We now substitute the fluid velocity derivative from (6.2) and obtain

$$F_b(\boldsymbol{k}) = \left(\frac{\alpha}{1 - \alpha}\right)\mathrm{Re}\{u_j^*(\boldsymbol{k})\left(-\mathrm{i}k_j P(\boldsymbol{k}) - \nu k^2 u_j(\boldsymbol{k})\right.$$
$$\left. - \alpha g \delta_{jz}\delta_{|\boldsymbol{k}|0} - g\delta_{jz}\delta_{|\boldsymbol{k}|0} + \alpha g \delta_{jz}\delta_{|\boldsymbol{k}|0}\right)\}. \tag{6.4}$$

Exploiting the fluid incompressibility, $k_j u_j(\boldsymbol{k}) = 0$, and the definition of the energy dissipation $D(k)$ at scale k, from (4.3), we obtain

$$F_b(k) = -\frac{\alpha}{1 - \alpha}D(k). \tag{6.5}$$

Therefore, an energy reduction through the bubbles is expected at all scales.

Note that, according to Einstein's relation (Landau & Lifshitz 1987, section 22), the viscosity of a suspension of spheres is higher than the viscosity of the original flow:

$$\eta = \eta_0\left(1 + \tfrac{5}{2}n\mathcal{V}_b\right),$$

where η_0 is the unperturbed viscosity, n is the number of spheres per unit volume and $\mathcal{V}_b$ is the volume of one sphere. On the other hand, in the case of uniformly distributed bubbles, the density decrease is given by

$$\rho = \rho_0(1 - n\mathcal{V}_b).$$

Thus the ratio $\nu = \eta/\rho$ increases compared to $\nu_0 = \eta_0/\rho_0$. In view of this derivation we can translate Saffman's argument on microparticles to bubbles as follows: small bubbles (if equidistributed) reduce the fluid density and increase the effective kinematic viscosity, and thus dissipate turbulent energy. We remark that in the case of heavy particles the increase of η with respect to η_0 is generally negligible compared to the density change.

6.4. *Numerical demonstration of the importance of bubble clustering*

We tested (6.5) by seeding the flow with $N_b = 288\,000$ bubbles ($\tau_b = \tau_k/10$ and $v_T = v_k$) at random positions. The bubbles are actively coupled to the flow, but they are not allowed to move from their initial position, in order to simulate a uniform bubble distribution. The void fraction is $\alpha \simeq 3.2\%$, therefore we expect a uniform reduction of the dissipation of the order of $0.03D(k)$ at all wavenumbers. The results for the spectrum of dissipation are shown in figure 11. We detect a relative reduction on all scales, except the large ones where the external forcing acts, that is in fairly
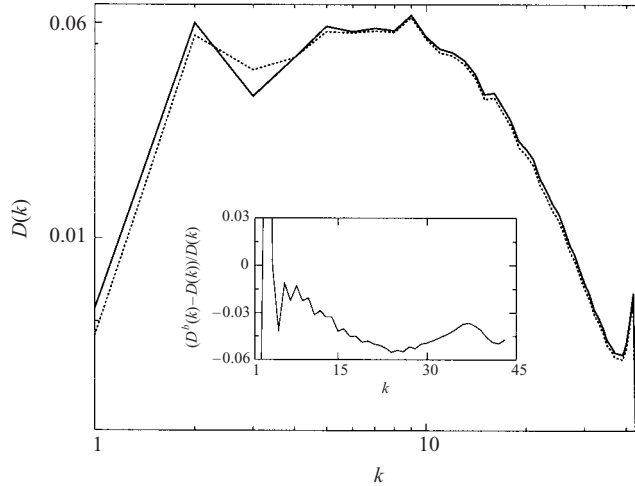
FIGURE 11. Dissipation spectra for one-phase turbulence, $D(k)$ (solid line), and two-phase turbulence with random uniform bubble distribution, $D^b(k)$ (dotted line). The inset shows the relative reduction of the dissipation, scale by scale, with respect to single-phase flow.

good agreement with the theoretical prediction. For the total dissipation the measured value is $\epsilon^b \simeq 0.98 \pm 0.04$, again consistent with the expected one.

The outcome of the test demonstrates the relevance of bubble accumulation. In fact, the energy dissipation reduction that we measure in two-way coupled flow (see §4 and in particular figure 3) is higher than could be justified by considering a uniform bubble distribution (with $\alpha \simeq 1.6\%$). Moreover, the modulation is selective in wavenumbers, and not uniform, as would be the case if (6.5) held. This is yet another indication of the importance of local bubble clustering.

7. Conclusions

The local distribution and the two-way interactions of microbubbles in homogeneous and isotropic turbulence have been investigated by direct numerical simulation. The Lagrangian–Eulerian approach has been employed. The analysis has been restricted to low void fractions, so that direct bubble–bubble interactions have not been considered. The forces acting on bubbles are fluid acceleration plus added mass effects, drag, gravity, and lift.

First we have addressed the one-way coupling regime in which bubbles do not transfer momentum to the flow. The bubble rise velocity in still water, v_T, has been kept constant and equal to the Kolmogorov velocity, v_k, and the response time, τ_b, has been changed according to $0.1\tau_k \leqslant \tau_b \leqslant \tau_k$. We have measured intense clustering in high-enstrophy regions, and preferentially in eddy zones, with the strongest effect occurring when $\tau_b = \tau_k$. As we had already found in Mazzitelli *et al.* (2003), the bubble distribution is not symmetric with respect to the direction of gravity, but a larger number of bubbles is found in downflow regions. The main reason is the action of the lift force on rising bubbles.

Second, the two-way coupling regime has been investigated. In this case the bubble response time has been fixed, $\tau_b = \tau_k/10$, and the rise velocity varied, $v_k \leqslant v_T \leqslant 8v_k$. Under the (erroneous) assumption of a random uniform bubble distribution we could analytically derive that the action of microbubbles on the spectrum should be

dissipative and uniform at all wavenumbers, see (6.5). This result was confirmed by numerical simulation where we artificially fixed the bubbles in space, but let them still force the flow. In contrast, our full numerical simulation with bubbles moving according to their dynamical equation (2.6) shows that the modulation is selective in k-space: the small wavenumbers are attenuated and the large ones are enhanced. The spectral selective modification is due to the bubble clustering in downflow regions.

After summing on all wavenumbers, we had already established in Mazzitelli *et al.* (2003) that bubbles reduce the overall energy dissipation rate ϵ. The proposed physical explanation of the phenomenon again is that bubbles collect in downflow zones, owing to the lift force, and transfer momentum upwards, owing to buoyancy. As a result they smooth the vertical fluid velocity fluctuations and dissipate kinetic energy. Confirmations of this interpretation have been given by reporting several fluid observables and by performing simulations with two-way coupling with and without lift force. In the latter analyses clusters in downflow regions as well as dissipative bubble action on turbulence were no longer detected.

All these findings have a direct or indirect bearing on the three types of observables on which we have focused in the introduction: the bubble distribution, the spectral information, and the bubble rise velocity.

(i) The use of bubbles as passive tracers to select low-pressure regions has to be made with caution for the following reasons. (i) Microbubbles with diameter much smaller than the Kolmogorov scale cluster in high-vorticity regions, but not necessarily in low-pressure regions. In fact, from figure 2, we conclude that the bubble probability of sampling eddy and shear zones is the same. (ii) The effect on the flow is not negligible because of clustering. Moreover, the isotropy of the turbulence is affected by the asymmetric distribution of bubbles within the vortices.

(ii) Our finding that the large scales are energetically reduced whereas the small scales are enhanced is consistent with the experimental results of Lance & Bataille (1991). However that result was obtained for larger bubbles for which there may be an additional effect due the wake behind the bubble. That effect may also lead to the $E(k) \sim k^{-8/3}$ spectrum seen in those data. We do not have any indication for such scaling in our simulation with point-particles. The energy spectrum and its dependence on the bubble void fraction and bubble size has to be further tested experimentally. The modulation in wavenumber of the spectrum will give an indication of the action of the lift force. We are carrying out experimental work in order to clarify this issue.

(iii) The third observable that we focused on is the bubble rise velocity in turbulence. In qualitative agreement with the experiment by Poorte & Biesheuvel (2002), we find that it is reduced, an effect which can only be accounted for by including the lift in the model.

Appendix A. Velocity interpolation at the position of the bubble

In general, the bubbles are not located on the grid points where the flow velocity is known. Therefore, an interpolation scheme is required, as pointed out in §2.2. In this Appendix we demonstrate that the 13-point third-order Taylor series interpolation
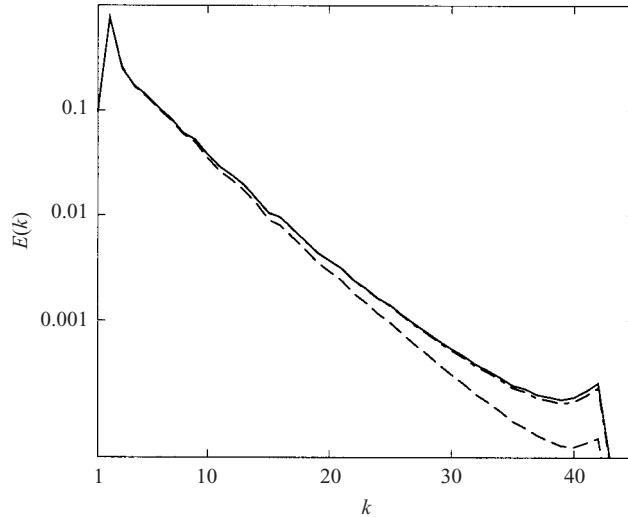
FIGURE 12. Energy spectrum computed on the grid (—) and on two staggered grids by linear (dashed) and 13-point (dot-dashed) interpolation.

employed (Yeung & Pope 1988) correctly represents the kinetic energy of the flow, including at large wavevectors.

In figure 12 the fluid energy spectrum

$$E(k) = \frac{1}{2} \sum_{k<|\boldsymbol{k}|<k+dk} u_i^*(\boldsymbol{k}) u_i(\boldsymbol{k})$$

is compared to the spectrum calculated on a staggered grid translated in each direction by half a mesh size. The velocity on this grid is computed by linear interpolation. A third grid is also considered and the velocity is interpolated on it by the third-order Taylor series based scheme. Several choices for the spacing of the third grid with respect to the original one have been taken into account and all of them lead to results analogous to the ones that we present. The plot shows that in the latter case most of the high-wavenumber energy is maintained, whereas in the former one it is not.

Appendix B. Quality of the point-force approximation

We can estimate whether the spurious effects on the fluid velocity, due to the point-force approximation introduced in §2.3, modify the results by performing the following test. We consider a flow with N_1 passive bubbles, and, at the same time, $N_2 = N_1$ active bubbles. Bubble trajectories are tracked and the absolute diffusions $\langle |\boldsymbol{x}(t) - \boldsymbol{x}_0|^2 \rangle$ are computed, separately for the two sets. Here $\boldsymbol{x}(t)$ is the position of the bubble at time t that was at $\boldsymbol{x}_0$ at time $t = 0$, and $\langle \cdot \rangle$ is the average over the sample. The motion of each bubble is advanced according to (2.6). The fluid velocity $\boldsymbol{u}$ in that equation depends, theoretically, on the fluctuations generated in the turbulent flow by all the bubbles, except the bubble's own perturbation. On the other hand, computationally, this specific fluctuation cannot be filtered from the underlying velocity field. The consequence is that the diffusion of the first set of bubbles (with one-way coupling) is correct, within our model, whereas the other diffusion (of bubbles with two-way coupling) is approximate. This can be used in
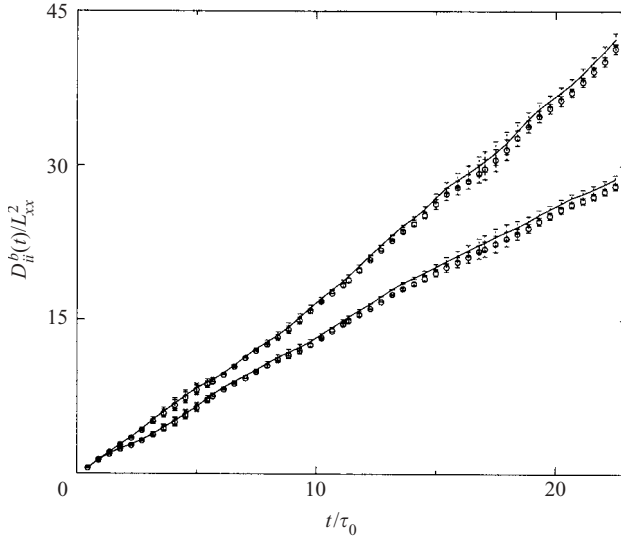
FIGURE 13. Diffusion in the z (upper curves) and average in the x, y-directions (lower curves), with error bars. The error bars are estimated starting from the relative error: $\epsilon = |(D_{xx}^b(t) - D_{yy}^b(t))/(D_{xx}^b(t) + D_{yy}^b(t))|$. The diffusion is shown for both sets of bubbles, with one- (open circles) and two-way (solid line) coupling.

order to measure how well the 'perturbed' equation (with the 'dirty' fluid velocity at the bubble location) resembles the one that we wish to integrate (with the velocity 'cleaned up' from the perturbation of the bubble itself). If we remove (or estimate as negligible) the bubble's own perturbation on the velocity, all bubbles, either active or passive, move in the same flow field and respond to the same equation of motion. Therefore their diffusions have to be consistent.

We now check whether this is the case to validate the approximation of $\boldsymbol{u}$ in (2.6) by the full velocity field. We define the diffusion tensor as

$$D_{ij}^b(t) = \langle (\boldsymbol{x}_i(t) - \boldsymbol{x}_{i0})(\boldsymbol{x}_j(t) - \boldsymbol{x}_{j0}) \rangle, \quad i, j = x, y, z.$$

In figure 13 the bubble diffusion in the (x, y)-plane and in the z (gravity) direction are presented. The error bars are estimated by the difference between results in the x- and y-directions, which, for symmetry reasons, are the same. The relative error is

$$\epsilon = \left| \frac{D_{xx}^b(t) - D_{yy}^b(t)}{D_{xx}^b(t) + D_{yy}^b(t)} \right|.$$

The parameters of the simulations are $\tau_b = \tau_k/10$ and $v_T = 8v_k$. The number of bubbles is $N_1 = N_2 = 144\,000$. The value of the rise velocity v_T and thus the strength of the forcing through the bubbles is the highest of all simulations presented throughout this work. In the case of successful validation, all cases with smaller forcing strength are therefore automatically included.

The result of the validation is that indeed $D_{ii}^b(t)$ is the same for the active and passive case (within the error), see figure 13. We conclude that the point-force approximation does not modify the bubble behaviour, within our numerical accuracy.
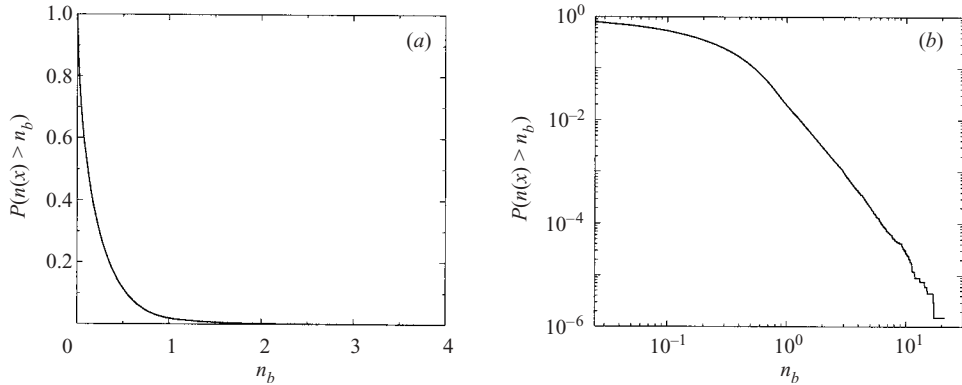
FIGURE 14. Probability that more than n_b bubbles are found inside the same computational cell, as a linear plot (*a*) and as a double-logarithmic plot (*b*). $P(n(\boldsymbol{x}) > 0) = 1$ by definition. The probability is estimated by the number of computational cells in which there are more than n_b bubbles normalized by the total number of cells occupied by the bubbles. Note that fractional values of n_b are due to the linear projection of each bubble (that is in general located between the grid points) to the eight nearest grid points.

Appendix C. Comment on neglecting direct bubble–bubble interactions

The turbulence modification is linked to bubble clustering in particular flow regions. Figure 2 shows that, for $\tau_b = \tau_k/10$, the ratio of the fraction of the total number of bubbles in eddy zones to the fraction of the total volume filled by eddies is order 2. However, within eddies, a very high local concentration can be achieved. In this Appendix we quantify this effect.

Up to 20 bubbles can be found in one computational cell in the two-way coupling case (for $\tau_b = \tau_k/10$ and $v_T = v_k$). These events, however, are extremely rare. Figure 14 shows a plot of the relative probability of finding more than n_b bubbles within the same computational cell. The ratio of grid cells with more than one bubble to all grid cells with any bubble contribution at all (which can be smaller than 1 as the weight of the bubbles is distributed over neighbouring cells) is about 0.02, and therefore we consider direct interactions negligible. Similar results also hold for the other runs with two-way coupling.

We finally note that clustering is strongly enhanced for $\tau_b \to \tau_k$. Indeed, our choice of a small bubble response time $\tau_b = \tau_k/10 \ll \tau_k$ is also driven by the need to reduce local bubble accumulation.

REFERENCES

AUTON, T. R. 1987 The lift force on a spherical body in a rotational flow. *J. Fluid Mech.* **183**, 199–218.

AUTON, T. R., HUNT, J. & PRUD'HOMME, M. 1988 The force exerted on a body in inviscid unsteady non-uniform rotating flow. *J. Fluid Mech.* **197**, 241–257.

BATCHELOR, G. K. 1967 *An Introduction to Fluid Dynamics.* Cambridge University Press.

BENZI, R., BIFERALE, L., CILIBERTO, S., STRUGLIA, M. V. & TRIPICCIONE, R. 1996 A generalised scaling of fully developed turbulence. *Physica* D **96**, 162–181.

BENZI, R., CILIBERTO, S., TRIPICCIONE, R., BAUDET, C., MASSAIOLI, F. & SUCCI, S. 1993 Extended self-similarity in turbulent flows. *Phys. Rev.* E **48**, R29–R32.

BOIVIN, M., SIMONIN, O. & SQUIRES, K. 1998 Direct numerical simulation of turbulence modulation by particles in isotropic turbulence. *J. Fluid Mech.* **375**, 235–263.

BUNNER, B. & TRYGGVASON, G. 1999 Direct numerical simulations of three-dimensional bubbly flows. *Phys. Fluids* **11**, 1967–1969.

CADOT, O., DOUADY, S. & COUDER, Y. 1995 Characterization of the low-pressure filaments in a 3-dimensional turbulent shear-flow. *Phys. Fluids* **7**, 630–646.

CHANG, E. J. & MAXEY, M. R. 1994 Unsteady flow about a sphere at low to moderate Reynolds number. Part 1. Oscillatory motion. *J. Fluid Mech.* **277**, 347–379.

CHANG, E. J. & MAXEY, M. R. 1995 Unsteady flow about a sphere at low to moderate Reynolds number. Part 2. Accelerated motion. *J. Fluid Mech.* **303**, 133–153.

CLIFT, R., GRACE, J. R. & WEBER, M. E. 1978 *Bubbles, Drops and Particles*. Academics.

CLIMENT, E. 1996 Dispersion de bulles et modification du mouvement de la phase porteuse dans des ecoulements tourbillonnaires. PhD thesis, Inst. Nat. Polytech, Toulouse.

CLIMENT, E. & MAGNAUDET, J. 1997 Simulation of bubble-induced flows in a liquid initially at rest. *C. R. Acad. Sci. Paris* **324**, 91–98.

CLIMENT, E. & MAGNAUDET, J. 1999 Large-scale simulations of bubble-induced convection in a liquid layer. *Phys. Rev. Lett.* **82**, 4827–4830.

DRUZHININ, O. A. 2001 The influence of particle inertia on the two-way coupling and modification of isotropic turbulence by microparticles. *Phys. Fluids* **13**, 3738–3755.

DRUZHININ, O. A. & ELGHOBASHI, S. 1998 Direct numerical simulations of bubble-laden turbulent flows using the two-fluid formulation. *Phys. Fluids* **10**, 685–697.

DRUZHININ, O. A. & ELGHOBASHI, S. E. 1999 On the decay rate of isotropic turbulence laden with microparticles. *Phys. Fluids* **11**, 602–610.

DRUZHININ, O. A. & ELGHOBASHI, S. 2001 Direct numerical simulation of a three-dimensional spatially developing bubble-laden mixing layer with two-way coupling. *J. Fluid Mech.* **429**, 23–61.

ELGHOBASHI, S. & TRUESDELL, G. 1993 On the two-way interaction between homogeneous turbulence and dispersed solid particles. I: Turbulence modification. *Phys. Fluids* A **5**, 1790–1801.

FERRANTE, A. & ELGHOBASHI, S. 2003 On the physical mechanisms of two-way coupling in particle-laden isotropic turbulence. *Phys. Fluids* **15**, 315–329.

FRIEDMAN, P. D. & KATZ, J. 2002 Mean rise of droplets in isotropic turbulence. *Phys. Fluids* **14**, 3059–3073.

GROSSMANN, S. & LOHSE, D. 1992 Intermittency in the Navier-Stokes dynamics. *Z. Phys.* B *Condensed Matter* **89**, 11–19.

GROSSMANN, S., LOHSE, D. & REEH, A. 1997a Different intermittency for longitudinal and transversal turbulent fluctuations. *Phys. Fluids* **9**, 3817–3825.

GROSSMANN, S., LOHSE, D. & REEH, A. 1997b Application of extended self similarity in turbulence. *Phys. Rev.* E **56**, 5473–5478.

HADAMARD, J. S. 1911 Mouvement permanent lent d'une sphere liquide et visqueuse dans un liquide visqueux. *C.R. Acad. Sci. Paris* **152**, 1735–1738.

HUNT, J. C. R., PERKINS, R. J. & FUNG, J. C. H. 1997 Review of the problems of modeling disperse two-phase flows. *Multiphase Sci. Technol.* **8**, 595–643.

KUMAR, S., MOSLEMIAN, D. & DUDUKOVIC, M. 1997 Gas-holdup measurements in bubble columns using computed tomography. *AIChE J.* **43**, 1414–1425.

LANCE, M. & BATAILLE, J. 1991 Turbulence in the liquid phase of a uniform bubbly air-water flow. *J. Fluid Mech.* **222**, 95–118.

LANDAU, L. D. & LIFSHITZ, E. M. 1987 *Fluid Mechanics*. Pergamon.

LA PORTA, A., VOTH, G. A., MOISY, F. & BODENSCHATZ, E. 2000 Using cavitation to measure statistics of low-pressure events in large-Reynolds-number turbulence. *Phys. Fluids* **12**, 1485–1496.

LEGENDRE, D. & MAGNAUDET, J. 1998 The lift force on a spherical bubble in a viscous linear shear flow. *J. Fluid Mech.* **368**, 81–126.

LOHSE, D. & MÜLLER-GROELING, A. 1995 The bottleneck effect in turbulence: Scaling phenomena in r-space versus p-space. *Phys. Rev. Lett.* **74**, 1747–1750.

LOHSE, D. & MÜLLER-GROELING, A. 1996 Anisotropy and scaling corrections in turbulence. *Phys. Rev.* E **54**, 395–405.

LOHSE, D. & PROSPERETTI, A. 2003 Controlling bubbles. *J. Phys.: Condens. Matter* **15**, S415–S420.

L'VOV, V. S., OOMS, G. & POMYALOV, A. 2003 Effect of particle inertia on the turbulence in a suspension. *Phys. Rev.* (E) (in press).

MAGNAUDET, J. & EAMES, I. 2000 The motion of high-Reynolds number bubbles in inhomogeneous flows. *Annu. Rev. Fluid Mech.* **32**, 659–708.

MAGNAUDET, J., RIVERO, M. & FABRE, J. 1995 Accelerated flows past a rigid sphere or a spherical bubble. *J. Fluid Mech.* **284**, 97–135.

MARCHIOLI, C. & SOLDATI, A. 2002 Mechanisms for particle transfer and segregation in turbulent boundary layer. *J. Fluid Mech.* **468**, 283–315.

MAXEY, M., CHANG, E. & WANG, L. 1994 Simulation of interactions between microbubbles and turbulent flows. *Appl. Mech. Rev.* **46**, 6-2, S70–S74.

MAXEY, M., PATEL, B., CHANG, E. & WANG, L. 1997 Simulations of dispersed turbulent multiphase flow. *Fluid Dyn. Res.* **20**, 143–156.

MAXEY, M. & RILEY, J. 1983 Equation of motion for a small rigid sphere in a nonuniform flow. *Phys. Fluids* **26**, 883–889.

MAZZITELLI, I. M., LOHSE, D. & TOSCHI, F. 2003 The effect of microbubbles on developed turbulence. *Phys. Fluids* **15**, L5–L8.

MEI, R., KLAUSNER, J. F. & LAWRENCE, C. J. 1994 A note on the history force on a spherical bubble at finite Reynolds number. *Phys. Fluids* **6**, 418–420.

MEI, R., LAWRENCE, C. & ADRIAN, R. 1991 Unsteady drag on a sphere at finite Reynolds number with small fluctuations in the free-stream velocity. *J. Fluid Mech.* **233**, 613–631.

MICHIYOSHI, I. & SERIZAWA, A. 1986 Turbulence in two-phase bubbly flow. *Nucl. Engng Des.* **95**, 253–267.

MONIN, A. S. & YAGLOM, A. M. 1975 *Statistical Fluid Mechanics.* The MIT Press.

MUDDE, R. F., GROEN, J. S. & VAN DEN AKKER, H. E. A. 1997 Liquid velocity field in a bubble column: Lda experiments. *Chem. Engng Sci.* **52**, 4217–4224.

MUDDE, R. F. & SAITO, T. 2001 Hydrodynamical similarities between bubble column and bubbly pipe flow. *J. Fluid Mech.* **437**, 203–228.

OOMS, G., GUNNING, J., POELMA, C. & WESTERWEEL, J. 2002 On the influence of the particles-fluid interaction on the turbulent diffusion in a suspension *Intl J. Multiphase Flow* **28**, 177–197.

POORTE, R. E. G. & BIESHEUVEL, A. 2002 Experiments on the motion of gas bubbles in turbulence generated by an active grid. *J. Fluid Mech.* **461**, 127–154.

RENSEN, J., BOSMAN, D., MAGNAUDET, J., OHL, C. D., PROSPERETTI, A., TÖGEL, R., VERSLUIS, M. & LOHSE, D. 2001 Spiraling bubbles: How acoustic and hydrodynamic forces compete. *Phys. Rev. Lett.* **86**, 4819–4822.

RIBCZYNSKI, W. 1911 On the translating motion of a fluid sphere in a viscous medium. *Bull. Acad. Sci. Cracovie* **40**, 40–46.

RIGHTLEY, P. M. & LASHERAS, J. C. 2000 Bubble dispersion and interphase coupling in a free-shear flow. *J. Fluid Mech.* **412**, 21–59.

RIVERO, M., MAGNAUDET, J. & FABRE, J. 1991 New results on the forces exerted on a spherical body by an accelerated flow. *C.R. Acad. Sci. Paris* II **312**, 1499–1506.

SAFFMAN, P. G. 1962 On the stability of laminar flow of a dusty gas. *J. Fluid Mech.* **13**, 120–128.

SAFFMAN, P. G. 1973 On the settling speed of free and fixed suspensions. *Stud. Appl. Maths* **LII**, 115–127.

SENE, K. J., HUNT, J. C. R. & THOMAS, N. H. 1994 The role of coherent structures in bubble transport by turbulent shear flows. *J. Fluid Mech.* **259**, 219–240.

SERIZAWA, A., KATAOKA, I. & MICHIYOSHI, I. 1975a Turbulence structure in air-water bubbly flow. I. measuring techniques. *Intl J. Multiphase Flow* **2**, 221–233.

SERIZAWA, A., KATAOKA, I. & MICHIYOSHI, I. 1975b Turbulence structure in air-water bubbly flow. II. local properties. *Intl J. Multiphase Flow* **2**, 235–246.

SERIZAWA, A., KATAOKA, I. & MICHIYOSHI, I. 1975c Turbulence structure in air-water bubbly flow. III. transport properties. *Intl J. Multiphase Flow* **2**, 247–259.

SNYDER, W. & LUMLEY, J. 1971 Some measurements of particle velocity autocorrelation functions in a turbulent flow. *J. Fluid Mech.* **48**, 41–71.

SPELT, P. D. M. & BIESHEUVEL, A. 1997 On the motion of gas bubbles in homogeneous isotropic flow. *J. Fluid Mech.* **336**, 221–244.

SQUIRES, K. & EATON, J. 1990 Particle response and turbulence modification in isotropic turbulence. *Phys. Fluids* A **2**, 1191–1203.

SRIDHAR, G. & KATZ, J. 1995 Drag and lift forces on microscopic bubbles entrained by a vortex. *Phys. Fluids* **7**, 389–399.

SRIDHAR, G. & KATZ, J. 1999 Effect of entrained bubbles on the structure of vortex rings. *J. Fluid Mech.* **397**, 171–202.

SUNDARAM, S. & COLLINS, L. 1999 A numerical study of the modulation of isotropic turbulence by suspended particles. *J. Fluid Mech.* **379**, 105–143.

TAYLOR, G. I. 1928 The forces on a body placed in a curved of converging stream of fluid. *Proc. R. Soc. Lond.* A **120**, 260–283.

THOMAS, N. H., AUTON, T. R., SENE, K. J. & HUNT, J. C. R. 1984 Entrapment and transport of bubbles in plunging water. In *Gas Transfer at Water Surfaces* (ed. W. Brutsaert & G. H. Jurka), p. 255. D. Reidel.

WANG, L. & MAXEY, M. 1993a The motion of microbubbles in a forced isotropic and homogeneous turbulence. *App. Sci. Res.* **51**, 291–296.

WANG, L. & MAXEY, M. 1993b Settling velocity and concentration distribution of heavy particles in homogeneous isotropic turbulence. *J. Fluid Mech.* **256**, 27–68.

VAN WIJNGAARDEN, L. 1998 On pseudo turbulence. *Theor. Comput. Fluid Dyn.* **10**, 449–458.

WRAY, A. A. & HUNT, J. C. R. 1990 Algorithms for classification of turbulent structures. In *Topological Fluid Mechanics* (ed. H. K. Moffatt & A. Tsinober), pp. 95–104. Cambridge University Press.

YANG, C. & LEI, U. 1998 The role of the turbulent scales in the settling of heavy particles in homogeneous isotropic turbulence. *J. Fluid Mech.* **371**, 179–205.

YEUNG, P. K. & POPE, S. B. 1988 An algorithm for tracking fluid particles in numerical simulations of homogeneous turbulence. *J. Comput. Phys.* **79**, 373–416.